12-31-2005

AFCI Quarterly Input – UNLV October 1 through December 31, 2005

Harry Reid Center for Environmental Studies. Nuclear Science and Technology Division

AFCI Quarterly Input – UNLV
October 1 through December 31, 2005

1.0 University of Nevada, Las Vegas (UNLV)

UNLV Transmutation Research Program. The University of Nevada, Las Vegas supports the AFCI through research and development of technologies for economic and environmentally sound refinement of spent nuclear fuel. The UNLV program has four components: infrastructure, international collaboration, student-based research, and management and program support. Management and program support highlights are the following:

- Information was submitted to North Carolina State University to include UNLV in the next issue of the Nuclear Engineering Sourcebook, which NCSU publishes for the Nuclear Engineering Department Heads Organization (NEDHO).
- Students and faculty staffed a nuclear educational and informational booth at the Town of Pahrump Fall Festival Oct. 1 and 2.
- Darlene Hoffman visited UNLV on Oct. 6 and met with the Radiochemistry program students and faculty.
- John Ashford gave a seminar on Oct. 25 in which he shared his thoughts on the politics of the nuclear power industry.
- Ralf Sudowe, Lawrence Berkeley National Laboratory, gave a seminar at UNLV on Nov. 3 entitled "Radiochemical separation techniques for the study of the heaviest elements."
- Tom Ward, consultant to DOE, visited UNLV from Nov. 15-18, 2005 for an end of the year review of the UNLV TRP program. He met with several program administrators and faculty members.
- Gordon Jarvinen, Los Alamos National Laboratory, gave a seminar at UNLV on Nov. 16 entitled "Separations Technology for Advanced Nuclear Fuel Cycles."
- Shuang Liu, Purdue University, gave a seminar at UNLV on Nov. 17 entitled "Chelated Radiometals for Heart and Tumor Imaging."
- David Costa, Los Alamos National Laboratory, gave a seminar at UNLV on Nov. 28.
- Steven Bakhtiar, Lawrence Berkeley National Laboratory, Radiochemistry Society President, gave a seminar at UNLV on Dec. 13 entitled "Sequential Isotopic Determination of Actinides in Low Level Samples."
- UNLV hosted a visit by AFCI program managers Buzz Savage and James Bresee from Dec. 14-15.
- TRP program director assisted the DOE in the development of research at the University of Nevada, Reno and accompanied AFCI program managers on a site visit to UNR on Dec. 16.

1.1 Infrastructure Augmentation

1.1.1 Infrastructure Augmentation Scope

The infrastructure augmentation component of the UNLV Transmutation Research Program enhances UNLV's research staff, facilities, and academic programs to increase the ability of the university to perform AFCI research.

1.1.2 Infrastructure Augmentation Highlights

- The TEM ceremonial grand opening was held Oct. 7. Student and faculty attendance was better than anticipated (around 75).

1.2 International Collaboration

1.2.1 International Collaboration Scope

The international collaboration component of the UNLV Transmutation Research Program enhances UNLV's breadth of scientific and scholastic experience. University collaboration is also an efficient conduit for international collaboration that benefits the national AFCI program. UNLV has ongoing relationships with the International Science and Technology Center (ISTC) who manages contracts with the Institute for Physics and Power Engineering (IPPE) in Obninsk, Russia for the TC-1 lead bismuth target loop and the Research Coordinative Center on the Problem of Muon Catalyzed Fusion and Exotic Quantum Systems (MUCATEX) in Moscow, Russia for the project entitled "Preparatory Work for the Systematic Measurements and Evaluation of Minor Actinide Nuclear Data." UNLV also has ongoing collaboration with the Ben Gurion University of the Negev in Beer Sheva, Israel (Task 19).

1.2.2 International Collaboration Highlights

- The Memorandum of Understanding and the Project Agreement (#3325p) for the new project "Preparatory Work for the Systematic Measurements and Evaluation of Minor Actinide Nuclear Data" were signed and submitted by UNLV in December. The program manager for MUCATEX is Leonid Ponomarev.
- An operational manual and safety reference for the IPPE TC-1 loop was completed.
- The work is in progress on 3-dimensional full core neutronic modeling of MgO-ZrO_2 fertile free fuel with previously selected most promising burnable poison designs by the collaborators at Ben Gurion University of the Negev.

1.3 Student Research

1.3.1 Student Research Scope

The Student Research component is the core of the UNLV Transmutation Research Program. The milestones, schedules, and deliverables of the student research projects are detailed in the individual research proposals. UNLV has 16 active student research tasks and 14 tasks that have concluded. The tasks are divided below in terms of their research area: fuels, separations, and transmutation sciences.

1.3.2 Student Research Highlights

FUELS TECHNOLOGY

Metallic Fuel Pins (Task 1) Highlights.

- Project completed in June 2004. Theses generated:

Xiaolong Wu, M.S., Mechanical Engineering, "Design and Analysis for Melt Casting Metallic Fuel Pins Incorporating Volatile Actinides," August 2002.
Taide Tan, M.S., Mechanical Engineering, "Design and Simulation of an Induction Skull Melting System," May 2004.

Remote Fuel Fabrication (Task 9) Highlights.

- Project completed in August 2004. See Task 22 for follow-on project. Thesis generated:

Jae-Kyu Lee, Ph.D., Department of Mechanical Engineering, "Three Dimensional Pattern Recognition using Feature-based Indexing and Rule-based Search," December 2003.

Interaction between Metal Fission Products and TRISO Coating Materials (Task 17) Highlights.

- Two experimental series were conducted of Pd deposition onto differently prepared SiC surfaces, investigating the samples both at UNLV and at the Advanced Light Source, Lawrence Berkeley National Laboratory.
- The first inverse photoemission (IPES) spectra were obtained with the newly commissioned experimental setup.

Dissolution, Reactor, and Environmental Behavior of ZrO_2-MgO Inert Fuel Matrix (Task 19) Highlights.

- The synthesis of the entire range of Zr to Mg, with Ce and Er concentrations being held at 5% and 2.5% respectively, has been completed with enough material for characterization and solubility studies.
- X-ray fluorescence has been performed on all ten batches to verify concentrations. X-ray diffraction has shown the range of Mg required for a single phase solid solution of cubic zirconia to be 10% to 28% Mg at current concentrations of Ce and Er.
- Pressure vessel experiments have begun. Acid dissolution studies suggest that it could be possible to leach uranium out of the ceramic without dissolving it. Therefore, these studies will be performed with uranium samples once they are prepared.
- The soxhlet studies have yielded quantitative data on water absorption, magnesium hydration, and corrosion of the ceramic.
- The work is in progress on 3-dimensional full core neutronic modeling of MgO-ZrO_2 fertile free fuel with previously selected most-promising burnable poison designs.

Design Concepts and Process Analysis for Transmuter Fuel Manufacturing (Task 22) Highlights.

- A systematic study was conducted seeking to arrive at an optimized plant configuration using value engineering techniques.
- A systematic analysis of plant reliability was conducted for multiple plant design configurations.

Impact of the Synthesis Process on Structure Properties for AFCI Fuel Candidates (Task 28) Highlights

- The sample preparation procedures for optical polarization microscopy, scanning electron microscopy (SEM), and transmission electron microscopy (TEM), were optimized using excess ZrN sample material from LANL. It was demonstrated that dimpling and ion-

milling is the method of choice for preparing multi-phased radioactive ceramic fuel samples.

- A new alternative TEM sample preparation procedure was also developed for brittle radioactive ceramic samples that are fragile to survive standard TEM sample preparation methods (polishing - dimpling – ion-milling, wedging – ion-milling). The electron-transparent radioactive nitride/oxide TEM fuel samples were produced using the ultra-microtome after mixing ground sample powder with Spurr resin, and radioactive nitride/oxide fuel samples were imaged at high resolution.
- The thermal behavior of ZrN inert matrix fuel samples were intensively studied by TGA/DSC and associated changes in phase constitution or structure by XRD Rietveld analysis and also by TEM. Under the influence of the TGA/DSC conditions, nearly all samples are affected by partial oxidation and the formation of Zr_2ON_2, associated by an about 1%-mass gain.
- An exothermic reaction at 1169°C was also observed by one of three samples and is not associated with the α-β phase transformation of ZrO_2. The α-β phase transformation of ZrO_2 at 1194°C is endothermic. However, the phase formation of Zr_2ON_2 and the slightly increased cubic ZrO_2 content in TGA/DSC treated samples does not negatively affect the nanostructure and the crystallinity of nitride ADS fuels and their physical properties will not deteriorate.
- Surrogate ADS nitride fuel pellets were synthesized through carbothermic reduction/nitridization using both (1) ball-milled oxide precursors as solid solutions in the system ZrO_2-UO_2-$ErO_{1.5}$, and (2) ball-milled (1-10 micron) stoichiometric mixtures of the oxides as purchased. None of the methods produced phase-pure mononitride solid solution samples. After using oxide solid solution precursor the formation of zirconium-enriched mononitride solid solutions and of uranium-enriched oxide/nitride solid solutions in the wt.-% ratios of 2:1 to 1:2 were observed.
- Applying direct-nitridization was not successful either. The formation of zirconium mononitride ZrN in these samples is a good indication of the significantly higher affinity of zirconium to nitrogen compared to the affinity of uranium to nitrogen. Uranium is present in a dioxide- or dinitride solid solution. In order to avoid this secondary phase formation the annealing procedure (5 h 1550°C in N_2 followed by 3 h at 1400°C in N_2/8%H_2 followed by 3 h at 1700°C in Ar/5%H_2) must be further improved and optimized.

SEPARATIONS TECHNOLOGY

Systems Engineering Model (Task 8) Highlights.

- Project completed in August 2004. See Task 24 for follow-on project. Thesis generated:

Lijian Sun, M.S., Mechanical Engineering, "Development of a Systems Engineering Model for Chemical Separation Process," December 2003.

Nuclear Criticality Analyses for Transmuter Fuel Fabrication and Reprocessing (Task 11) Highlights.

- Project completed in December 2004. Thesis generated:

Elizabeth Bakker, M.S., Mechanical Engineering Department, "Criticality and Thermal Analysis of Separated Actinides in Transmutation," November 2003.

Immobilization of Fission Iodine (Task 15) Highlights.

- Iodate reduction was measured by alkali lignin.
- Temperature and lignin concentration response for the reduction reaction response were measured.
- Methyl iodide decomposition rates were measured in the presence of various nucleophiles.
- The recovery of methyl iodide from the "preparative gas chromatograph" was demonstrated.

Fluorapatite Waste Forms (Task 16) Highlights.

- Project completed December 2005. Theses generated:

Chirantha Prageeth Rodrigo, M.S., Department of Chemistry, "Synthesis and Characterization of Strontium Fluorapatite," August 2005.

Gunanda Waduge Chinthaka Silva, M.S., Department of Chemistry, "Study on Immobilizing Radionuclides in Apatite-based Host Phase Materials," December 2005.

Development of Integrated Process Simulation System Model for Spent Fuel Treatment Facility Design (Task 24) Highlights.

- Process engineering modeling software, ASPEN-plus, can be accessed through the newly developed interface created within the TRPSEM package. Such integration completes the chemical separation simulation package that interacts with both chemical separation calculation (AMUSE) and process engineering software (ASPEN-plus). The system data generated from ASPEN-plus can be passed to AMUSE, while AMUSE separation results can feed through the interface as input information for the ASPEN-plus.
- A new separations flowsheet was developed after discussing with researchers from Argonne National Laboratory (ANL). The new process is for solidification of raffinates derived from the TRUEX, UREX and PUREX processes via steam reforming.

Electrochemical Separation of Curium and Americium (Task 25) Highlights.

- Measurements of the complexation of Ce with ligands including citrate, EDTA and NTA to expand the pH range accessible for examining the Ce^{3+}/Ce^{4+} redox couple have been concluded.
- The group has finished the initial polymer synthesis studies and has reduced Au into the membranes to attach the chelation species.
- The SEM analysis of the polymer and polymer/Au composites has been concluded.
- An additional electrochemical workstation has been purchased to expand the electrochemical measurement capabilities.

Fundamental Chemistry of U and Pu in the TBP-Dodecane-Nitric Acid System (Task 26) Highlights.

- Work this quarter focused on the determination of nitrate concentration. The HPLC was used for most of this study. This instrument was found to be precise, but not very reliable. It was then decided that IC would be a more efficient means of measuring nitrate.

- Methods to quantify the concentrations of hydroxylamine and acetic acid using High Performance Liquid Chromatography (HPLC) with UV-VIS Detection were performed. It was determined that hydroxylamine is not stable over time and is not retained long enough on any column for enough time for quantitative work-only qualitative. Acetic Acid is retained on the column under a variety of conditions. HPLC could be an acceptable method for determining acetic acid concentration.
- The complexation of AHA with uranium was evaluated by UV-Visible spectroscopy. Analyses of XAFS 3rd phase studies were performed.

Investigation of Optical Spectroscopy Techniques for On-Line Materials Accountability in the Solvent Extraction Process (Task 29) Highlights.

- The Laser Spectroscopy system was installed. Shakedown of system started.
- Investigation of the determination of uranium in aqueous streams continued.

Combined Radiation Detection Methods for Assay of Higher Actinides in Separation Processes (Task 30) Highlights

- The PI met with group leaders and technical staff at LANL in conjunction with the MPAC PI and others from Idaho State University to develop collaborations for monitoring systems development.
- As part of UNLV Task 6, assembly and programming of a new data acquisition system (DAQS) for the ^{3}He Neutron Multiplicity Detector System (NMDS) was completed and additional components were ordered.
- The NMDS was tested both with cosmic radiation (background counting) and with a weak ^{252}Cf source; results compared favorably with previous counting data.
- Students resumed developing concepts for combined neutron-gamma and passive-active interrogation systems using the NMDS.

TRANSMUTATION SCIENCES

Niobium Cavity Fabrication Optimization (Task 2) Highlights.

- Project completed in August 2005. Theses generated:

Qin Xue, M.S., Mechanical Engineering, "Modeling and Simulation of the Chemical Etching Process in Niobium Cavities," August 2002.

Sathish K. Subramanian, M.S., Mechanical Engineering, "Modeling, Optimization, and Flow Visualization of Chemical Etching Process in Niobium Cavities," December 2003.

Anoop George, M.S., Electrical and Computer Engineering Department, "Study of Secondary Electron Emission From Niobium at Cryogenic Temperatures," August 2005.

LBE Corrosion of Steel (Task 3) Highlights.

- Project completed in May 2004. See Task 18 for follow-on project. Thesis generated:

Daniel Koury, M.S., Physics Department, "Investigation of the Corrosion of Steel by Lead-bismuth Eutectic (LBE) Using Scanning Electron Microscopy And X-ray Photoelectron Spectroscopy," December 2002.

Environment-Induced Degradation and Crack-Growth Studies in Candidate Target Materials (Task 4) Highlights.

- Project completed in December 2004. Theses generated:

Ramprashad Prabhakaran, M.S., Mechanical Engineering, "Environment-Induced Degradations in a Target Structural Material for Transmutation Applications," August 2004.

Sudheer Sama, M.S., Mechanical Engineering, "Embrittlement and Localized Corrosion in Alloy HT-9," August 2004.

Phani P. Gudipati, M.S., Mechanical Engineering, "Stress Corrosion Cracking Resistance of Martensitic Stainless Steels for Transmutation Applications," December 2004.

Mohammad K. Hossain, Ph.D., Mechanical Engineering, "Stress Corrosion Cracking and Hydrogen Embrittlement of Martensitic Alloy EP-825," December 2004.

Venkataramakrishnan Selvaraj, M.S., Mechanical Engineering, "Environment Assisted Cracking of Target Structural Materials Under Different Loading Conditions," December 2004.

Modeling Corrosion in Oxygen-Controlled LBE Systems with Coupling of Chemical Kinetics and Hydrogen Transport (Task 5) Highlights.

- Project completed in August 2004. Theses generated:

Chao Wu, M.S., Mechanical Engineering, "Study of Geometry Effects on Local Corrosion Rates for LBE Loop," July 2003.

Kanthi K. Dasika, M.S., Mechanical Engineering, "Modeling Corrosion in Oxygen-Controlled LBE Systems with Coupling of Chemical Kinetics and Hydrogen Transport," November 2003.

Narain Armbya, M.S., Mechanical Engineering, "CFD Analysis of 3-D Thermalhydraulics Flow Effects on Wall Concentration Gradient Profiles for LBE Loop Fittings," December 2004.

Neutron Multiplicity Measurements of Target/Blanket Materials (Task 6) Highlights.

- This project will be ending as the Neutron Multiplicity Detector System will now be used in a new project to assay separations processing streams for Materials Protection, Accounting, and Control (TRP Task 30).
- The graduate student in computer engineering is working on her M.S. thesis and is expected to graduate in May 2006.

Development of Dose Conversion Coefficients for Radionuclides Produced in Spallation Neutron Sources (Task 7) Highlights.

- Project completed in August 2005. Theses generated:

John P. Shanahan, M.S., Health Physics, "Dose Coefficients for Radionuclides Produced in a Spallation Neutron Source," August 2003.

Yayun Song, M.S., Health Physics, "Investigation and Calculations of Dose Coefficients for Radionuclides Produced in a Spallation Neutron Source Using the ENSDF and NUBASE Nuclear Databases," May 2004.

Development of a Mechanistic Understanding of High-Temp Deformation of Alloy EP-823 for Transmutation Applications (Task 10) Highlights.

- Project completed in August 2004. Theses generated:

Srinivasa R. Kukatla, M.S., "Corrosion and High-Temperature Deformation Characteristics of a Target Structural Material for Transmutation Applications," June 2004.

Venkata Nagarjuna Potluri, M.S., "Effect of Heat Treatment on Deformation and Corrosion Behavior of Type 422 Stainless Steel," August 2004.

Bhagath Yarlagadda, M.S., "Elevated Temperature Mechanical Properties and Corrosion Characteristics Evaluation of Alloy HT-9," August 2004.

Radiation Transport Modeling using Parallel Computational Techniques (Task 12) Highlights.

- Project completed in December 2004. Thesis generated:

Suresh B. Sadineni, M.S., Mechanical Engineering, "Benchmarking Photoneutron Production of MCNPX Simulations with Experimental Results," December 2002.

Developing a Sensing System for the Measurement of Oxygen Concentrations in Liquid LBE Systems (Task 13) Highlights.

- Project completed in August 2005. Thesis generated:

Ramkumar Sivaraman, M.S., Electrical and Computer Engineering, "Calibration of YSZ Sensor for the Measurement of Oxygen Concentration in Liquid PBE," December 2003.

Use of Positron Annihilation Spectroscopy for Stress-Strain Measurements (Task 14) Highlights.

- Cylindrical specimens of Alloys EP-823, HT-9 and 422, tested at different levels of tensile loading, have been analyzed by pair-production, activation and neutron diffraction techniques for characterization of residual stress resulting from plastic deformation due to applied loads between the yield strength and the ultimate tensile strength.
- The residual stress in terms of the S-parameter was gradually enhanced with increasing levels of plastic deformation at higher applied stresses. Conversely, the magnitude of the W and T-parameter was gradually reduced with increasing applied stress indicating higher residual stress in the tested specimens.

Corrosion Mechanisms and Kinetics of Steels in Lead-Bismuth Eutectic (Task 18) Highlights.

- Power and air conditioning renovations were started in the High Temperature Materials Experimental Facility.
- TEM and WDS (wavelength-dispersed spectroscopy) investigations were completed on the corrosion of D-9 steel by LBE.
- Assembly of laser Raman system was completed. Data acquisition on standards and unknowns was started.

Impact of Silicon on Corrosion Resistance of Stainless Steels in LBE Systems (Task 20) Highlights.

- Tensile properties of T91 grade steel with 1 and 2 wt% Si content were evaluated at temperatures ranging between ambient and 550^{o}C.
- The stress-strain diagrams obtained in stress corrosion cracking testing under a slow-strain-rate (SSR) condition indicate enhanced cracking susceptibility at elevated temperatures.
- The results of localized corrosion studies by cyclic potentiodynamic polarization technique exhibited an active-passive behavior with a positive hysteresis loop.

- Fractographic evaluations were performed on cylindrical specimens used in SSR testing by scanning electron microscopy.

Oxide Film Growth Modeling in LBE Systems (Task 21) Highlights.

- The numerical simulations on the enhancement of oxygen transport by forced convection using the Lattice Boltzmann method were performed.
- The general kinetics of oxidation associated with scale removal such as scale dissociation, volatilization, erosion, or mass transfer corrosion using the dimensionless Tedmon's equation were studied and analyzed.

Corrosion Barrier Development for LBE Corrosion Resistance (Task 23) Highlights.

- The chromium nanowire coverage problem was experimentally investigated but could not be resolved.
- Nickel was chosen as the alternative material to replace chromium after investigation confirmed effectiveness as a filler and anticorrosion material.
- Test experiments are currently being planned.

Reactor Physics Studies for the AFCI RACE Project (Reactor-Accelerator Coupling Experiments Project (Task 27) Highlights.

- UNLV received the RELAP5 code system for thermal-hydraulic reactor analysis from INL.
- UNLV received a license for the ERANOS/APOLLO code system for thermal-hydraulic reactor analysis from CEA (France).
- Students completed their final design report for their senior design project for a water-cooled high power target for High-Power RACE. During their presentation they displayed rapid-prototype models of the target that they had fabricated in the UNLV machine shop. The models included mockups of separate tungsten, aluminum, and uranium components and a cut-away to demonstrate the machining and sealing of cooling channels.

1.3.3 Student Research Technical Summary

FUELS TECHNOLOGY

Interaction between Metal Fission Products and TRISO Coating Materials (Task 17).

The objective of this project is to study the influence of fission products (currently in particular Pd) on the chemical and electronic properties of the SiC coating layer in TRISO nuclear fuel particles. For this purpose, a suite of different spectroscopic techniques are utilized that give direct insight into the chemical bonding, the electronic states in the valence and conduction bands (and hence the band gap), and long-range electron transfer and diffusion information. At UNLV, techniques are utilized that are surface sensitive, such as X-ray photoelectron spectroscopy (XPS), UV photoelectron spectroscopy (UPS), and inverse photoemission (IPES), while at the Advanced Light Source, Lawrence Berkeley National Lab, methods are utilized that are sensitive to the surface-near bulk (X-ray emission (XES) and absorption (XAS) spectroscopy). For structural information, the samples described below are currently also being

investigated with TEM for cross-sectional studies. Furthermore, the group has just ordered an ultra-high vacuum scanning probe microscope which will be connected to the existing four-chamber system at UNLV and which will allow the detailed local study of the two-dimensional surface structure with Atomic Force Microscopy, Scanning Tunneling Microscopy, Scanning Tunneling Spectroscopy, and Kelvin Probe Force Microscopy without intermittent air exposure. This instrument is expected to be available for experiments by June 2006.

In the past quarter, the group focused on augmenting their knowledge of the Pd/SiC interface formation from their previous study of the interface between a thin film of evaporated Pd and a *well-ordered* single crystal 6H-SiC(0001) surface, formed at *room temperature*. In that series, it was found that the presence of two distinct carbon species on the SiC surface and three species at the Pd/SiC interface indicate both a short-range charge transfer as well as diffused species. Furthermore, they found charge transfer from the Pd to the upper valence band localized near the Si atoms, giving the SiC layer a more "metallic" character. In order to shed more light on these processes and also to make them more directly applicable to SiC layers in TRISO particles, two experimental series were performed in which (a) the Pd layer thickness was successively increased, and each step monitored by XPS and UPS, (b) the SiC surface was cleaned and structurally disordered by extensive Ar-ion sputtering with 2 keV ions in order to mimic the fact that TRISO SiC layers are not single-crystalline, and (c) the interface was formed at room temperature (series 1) and at the currently highest attainable temperature in our system (series 2, approx. 800^{o}C).

In addition to the intermittent sample analysis with XPS and UPS, a-posteriori XES and XAS experiments were performed at the Beamline 8.0 at the ALS for the two completed interface samples. The data analysis is currently in progress, and involves calibration and sophisticated multi-spectra peak fitting. As an example of the experimental data, Figure 1 shows a sequence of C 1s XPS spectra, obtained from series 2, i.e., the interface sample grown at approx. 800^{o}C. As labeled on the right hand side, the spectra correspond to the as-introduced SiC single crystal surface (bottom spectrum), the sample after prolonged Ar ion sputter-cleaning (and roughening), and after each Pd deposition step.

For the trained eye, the spectra in Figure 1 change significantly as a function of sample treatment. During the sputter treatment, adventitious carbon (and oxygen, not shown) is removed, which can be seen by the absence of the peak at 282 eV in the spectrum following the sputter-cleaning. Upon deposition of Pd, two major effects are visible, first a shift of the main peak towards smaller binding energies, most likely due to a long-range charge transfer (as is commonly found in the preparation of Schottky contacts). Secondly, one finds the emergence of additional carbon species, as indicated by the oval in Figure 1. In the topmost spectrum (i.e., the thickest Pd film), a strongly different C 1s peak shape is found.

As mentioned above, a multi-spectra peak fit analysis is currently being performed. This fit is complicated due to the need for fitting all spectra simultaneously to ensure that the results for each spectrum can be directly compared (same separation between the species, same line width, etc.) and hence to ensure that quantitative information about the emergence of the new species can be obtained. It will also be the outcome of the fit whether the data can be convincingly described with two or three different carbon species at the Pd/SiC interface.

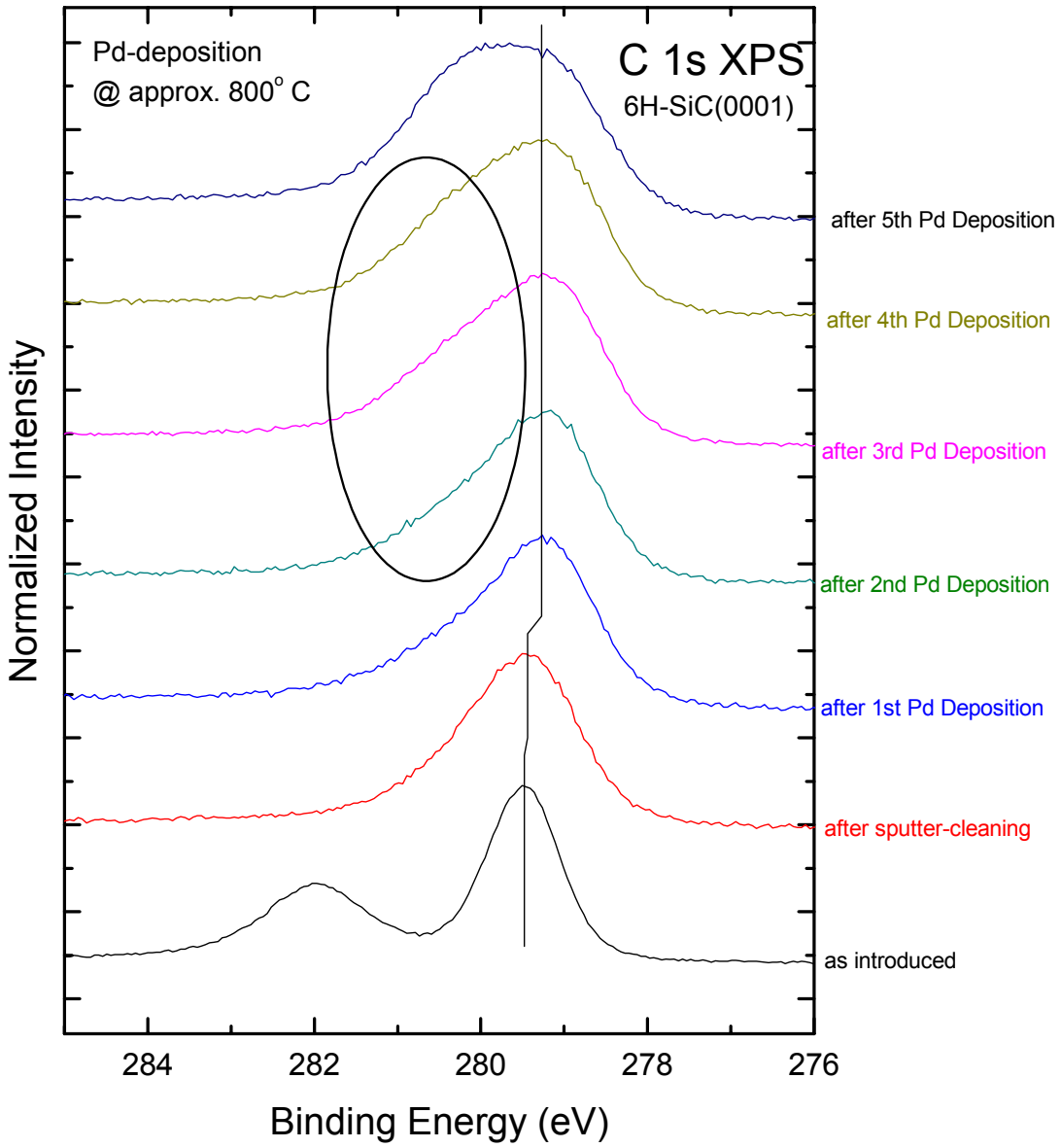

Figure 1. XPS spectra of an as-introduced SiC-6H(0001) single crystal surface, after 2 keV Ar^+ ion sputtering, and after several Pd deposition steps at approx. 800°C. The vertical line indicates the shift of the C 1s main peak, the oval indicates the spectral area in which additional C components are formed during the interface formation.

Further information can be obtained from other XPS core levels (such as the Pd $3d_{3/2}$ level in Figure 2) and from the XAS and XES spectra (not shown). The Pd spectra in Figure 2 do not show a significant variation in spectral shape, indicating that the distribution of different chemical Pd environments does not vary significantly as a function of Pd coverage. Nevertheless, a shift towards lower binding energy as a function of Pd coverage is clearly found,

which indicates the contribution of the Pd over layer in a long-range charge transfer, leading to a shift of the bands in SiC. Also, a final state screening effect may contribute to this shift. It will be the outcome of the current data analysis to determine the number and nature of chemical species at the interface, the work function (which can be derived from the UPS spectra), the band alignment, and other characteristics of the electronic and chemical properties of the interface. These, in turn, will help paint a first detailed picture of the Pd/SiC interface, which can then be tested by performing experiments on real TRISO SiC layers.

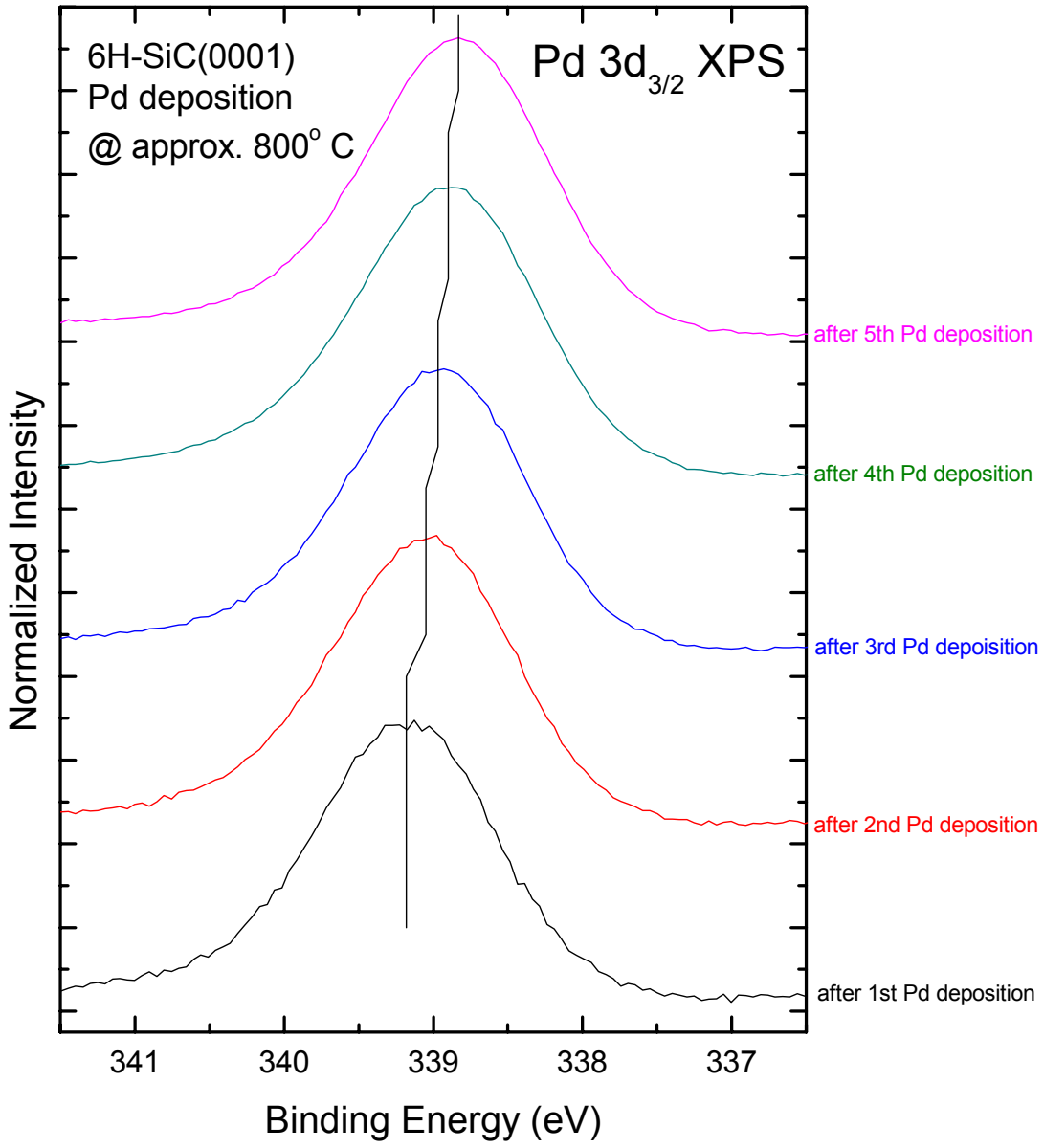

Figure 2. Pd $3d_{3/2}$ XPS spectra of the Pd/SiC interface formation at approx. 800° C. The vertical line indicates a reduced binding energy as a function of Pd over layer coverage.

Dissolution, Reactor, and Environmental Behavior of ZrO_2-MgO Inert Fuel Matrix (Task 19)

This project examines inert matrix fuels containing ZrO_2 and MgO as the inert matrix, with the relative amount of MgO varied from 30 % to 70 % in ZrO_2. Reactor physics calculations are used to examine suitable quantities of burnable poisons from the candidate elements Gd, Er, or Hf with reactor grade Pu providing the fissile component, with up to 10 % of ^{239}Pu. Ceramics are synthesized and characterized based on the reactor physics results. The solubility of the fuel ceramics, in reactor conditions, reprocessing conditions, and repository conditions, are investigated in a manner to provide thermodynamic data necessary for modeling.

The fuel matrix is designed based on neutronic properties, repository behavior, and reprocessing characteristics. The matrix should be as neutron transparent as possible. Burnable poisons are used to maintain constant reactivity. The matrix should also act as a suitable host form for fission products and actinides in a repository environment. Finally, the matrix should be compatible with reprocessing schemes under development in the advanced fuel cycle initiative.

Ceramic Fuel Synthesis and Characterization

The entire range of Mg to Zr from 0 – 92.5% with Ce at 5% and Er at 2.5% has been synthesized using the precipitation method previously described. It was shown that 10% Mg with 5% Ce, 2.5% Er and 82.5% Zr is enough to fully stabilize the Zirconia to a cubic structure and produce a single phase. From x-ray diffraction the maximum amount of Mg that can be incorporated into the Zr matrix with the Ce and Er is 28% Mg, after which a second Mg phase called periclase begins to build in. The sample shown in Figure 3 contains 30% Mg, 5% Ce, 2.5% Er, and 62.5% Zr and it shows the lowest unit cell parameter at 5.09885, which further supports this as the maximum amount of soluble Mg.

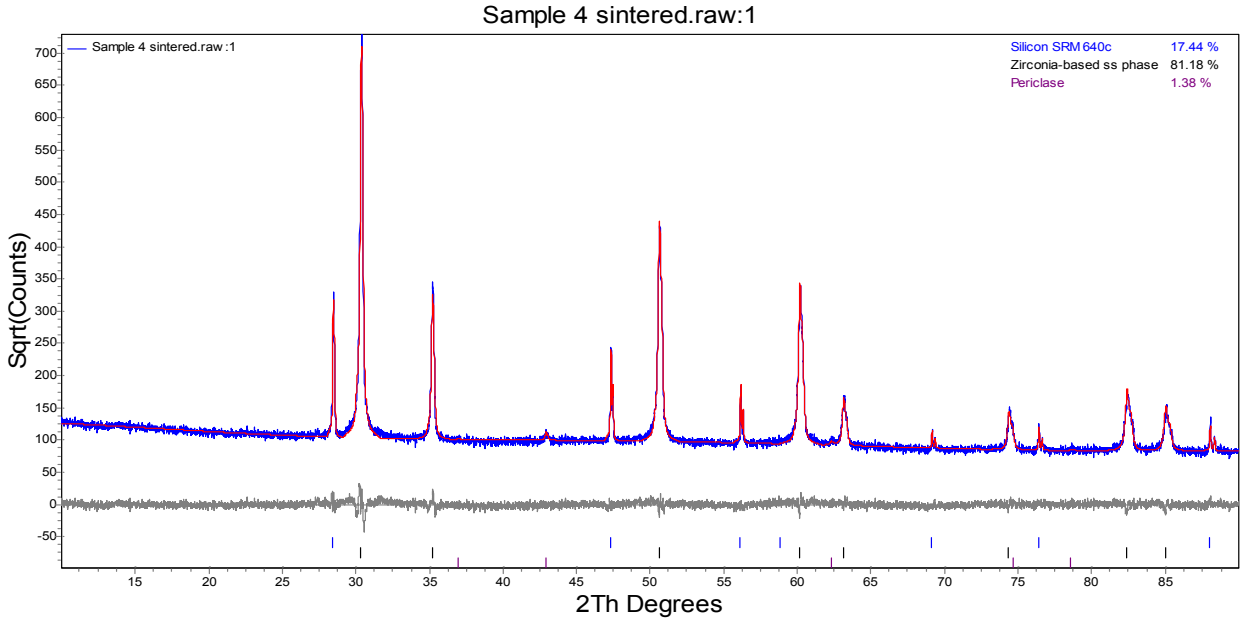

Figure 3. Rietveld analysis based on X-ray diffraction patterns of an inert matrix fuel sample containing 30% Mg, 5% Ce, 2.5% Er, and 62.5% Zr.

A Quantachrome Nova 1000 surface area analyzer was used to get the surface area of ceramic materials so that surface area can be related to solubility. A method is being developed for SEM imaging of sintered pellets. X-ray fluorescence has been performed on the entire range of material that has been synthesized to verify the concentration of the precipitant is consistent with that of the solution.

Pressure Vessel Method

Pressure vessel experiments are now underway. The Parr pressure vessel system was tested and initial results show ceramic degradation with solubility of the MgO phase.

Ceramic Solubility in Reprocessing Conditions

Alternatives for dissolving pellets have been insufficient in dissolving the entire pellet at high concentrations of Zr. However, when the pellet is crushed, Mg is leached into HNO_3, therefore it may be possible to leach out uranium from the crushed ceramic as well. Because of this, reprocessing experiments will be performed with uranium samples once they have been synthesized.

Soxhlet Solubility Studies

The soxhlet has produced information on corrosion properties, ability to absorb water, and the extent to which Mg is hydrated. A mass loss due to corrosion was not observed until the Mg content reached 60%; however, Mg was present in the water at trace levels (1 ppm) for Mg concentrations as low as 40%. Pellets were able to absorb 10% wt/wt water. The more flawed the pellet the greater its ability to retain water. It was also observed that Mg was hydrated in soxhlet conditions. This causes a mass gain and explains the evidence of corrosion in the water without a mass loss. An x-ray diffraction pattern shown in Figure 4 was taken of a sample (40% Mg, 5% Ce, 2.5% Er, and 52.5% Zr) that had been in the soxhlet for 1150 hours, which confirms the hydration of Mg by the presence of brucite [$Mg(OH)_2$].

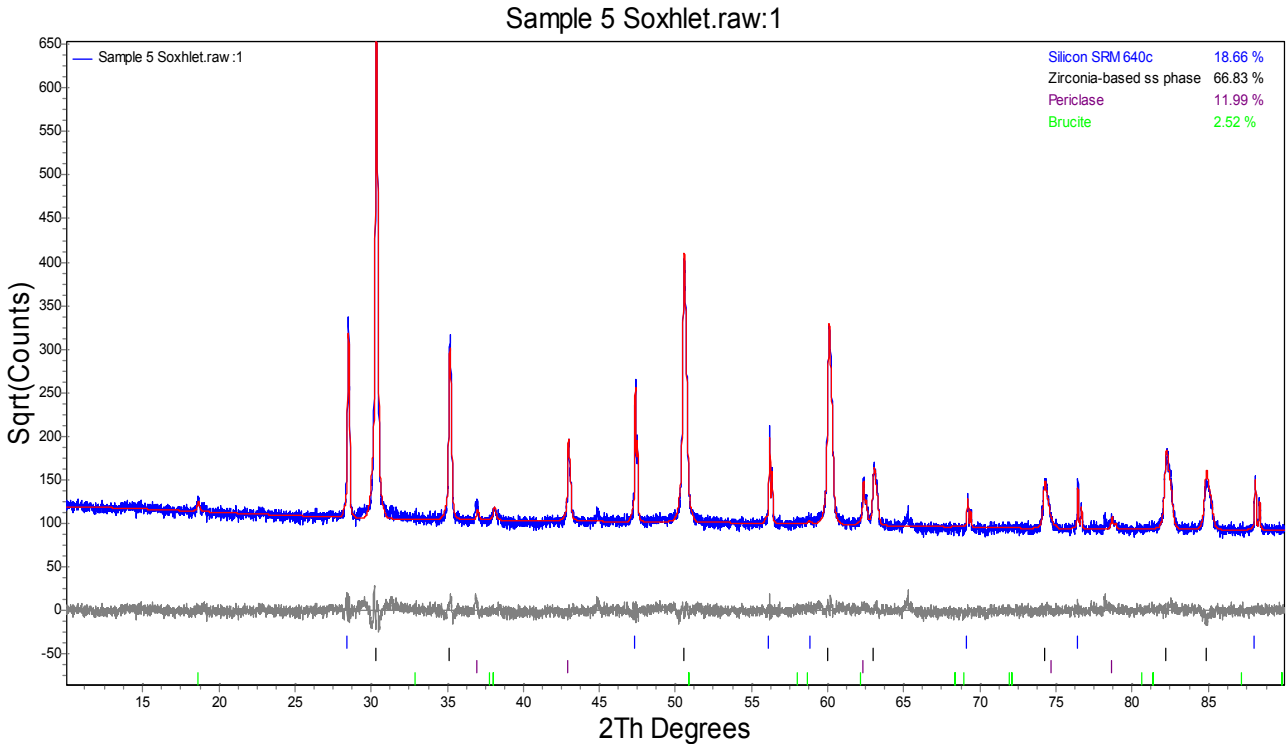

Figure 4. Rietveld analysis based on X-ray diffraction patterns of an inert matrix fuel sample containing 40% Mg, 5% Ce, 2.5% Er, and 52.5% Zr, which quantifies a new phase formation of brucite.

Reactor Physics Calculations

The work is in progress on 3-dimensional full core neutronic modeling of MgO-ZrO_2 fertile free fuel with previously selected most-promising burnable poison designs. In the initial stage of the full core modeling, the focus is to determine the Pu and burnable poison loading such that would ensure the core reactivity control and desired fuel cycle length. As a part of 3-dimensional full core analysis, the main analysis tool – SILWER computer code – was modified to account properly for thermal conductivity of the fuel. The original version of SILWER assumes UO_2 by default for all analyzed fuel types. Thermal conductivity of fertile free fuels varies greatly with the matrix material composition and differs from UO_2. As a result, the calculated average fuel temperature subsequently used for Doppler feedback calculations is calculated inaccurately. Moreover, the original version of the SILWER code accepts only solid fuel pellet geometry, which in case of annular pellets also results in inaccurate fuel temperature calculation. In the updated version of SILWER, the following modifications were made in the thermal-hydraulic feedback module of the code: Thermal conductivity of the fuel as a function of temperature is specified by user as a set polynomial coefficients. The temperature distribution of annular as well as solid fuel pellet geometries are calculated properly using ceramic data.

Two important limitations of the SILWER code with regards to the IMF analysis should be noted. During fuel temperature calculations, SILWER thermal-hydraulic module employs the thermal conductivity of UO_2. These data cannot be applied to IMF because the thermal

conductivity of IMF differ from UO_2 and depends on inert matrix material composition. The thermal-hydraulic module performs fuel temperature calculations assuming solid fuel pellet geometry even for the annular fuel. Thus, in order to adapt the SILWER code for simulation of a PWR core loaded with IMF several modifications to the SILWER code were made.

Figures 5 and 6 summarize graphically the effect of the fuel matrix thermal conductivity and fuel pellet geometry on the radial temperature distribution within the fuel pellet. All cases presented in the figures are plotted for identical linear power rating.

In summary, the results of calculations demonstrate the importance of using the actual thermal conductivity data and fuel pellet geometry. The use of thermal conductivity data of UO_2 for different inert matrix compositions and ignoring annular fuel pellet geometry introduces significant error into calculations.

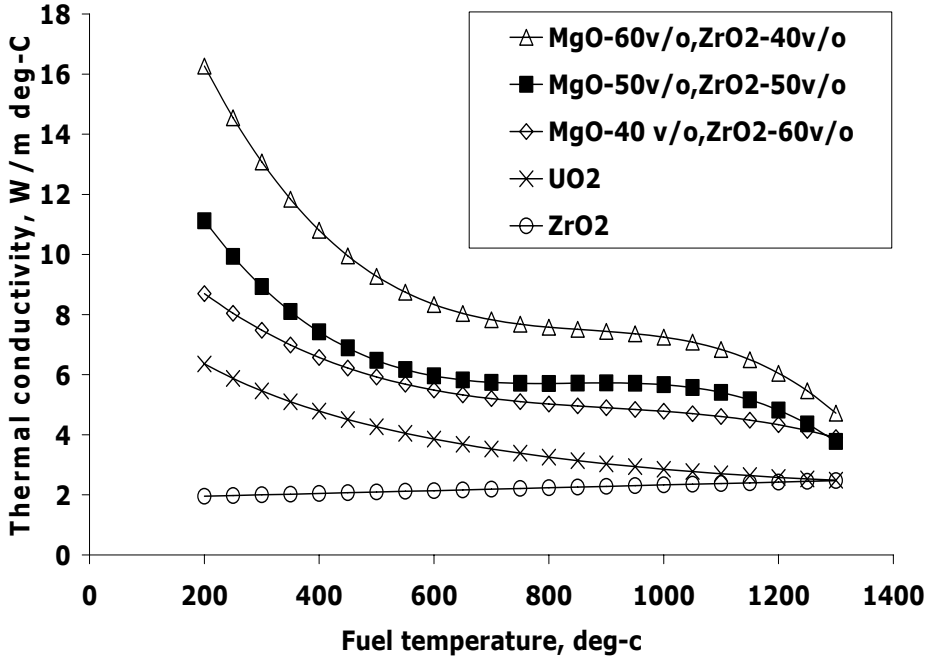

Figure 5. Thermal conductivity of various fuel matrices.

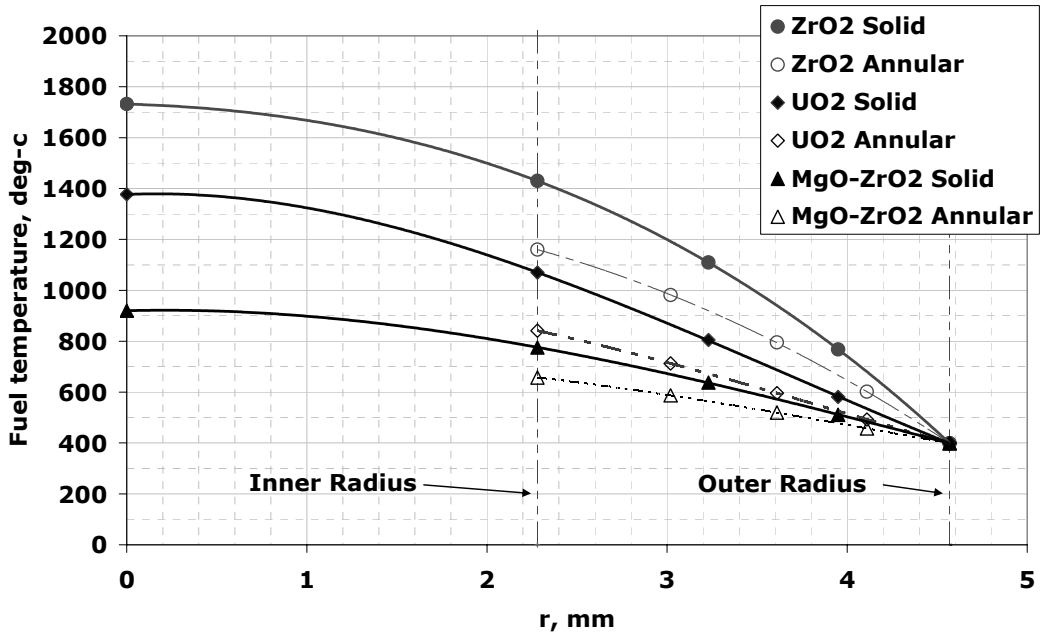

Figure 6. Radial fuel temperature distribution for different pellet geometries and fuel matrices.

Design Concepts and Process Analysis for Transmuter Fuel Manufacturing (Task 22)

Reliability of Individual Manipulators

The *failure density* function is defined as:

$$\dot{R}(t) = -f(t)$$

where *R(t)* is the item reliability
f(t) is the failure (or probability) density function

The *hazard rate* function is expressed as:

$$\lambda(t) = \frac{f(t)}{R(t)} = -\frac{\dot{R}(t)}{R(t)}$$

where $\lambda(t)$ is the item hazard rate or time depend failure rate

The *general reliability* function then results as:

$$R(t) = e^{-\int_0^t \lambda dt} = e^{-\lambda t}$$

Mean time to failure (MTTF) is expressed as:

$$MTTF = \int_0^\infty R(t)dt$$

For constant failure rates: $MTTF = \int_0^\infty e^{-\lambda t} dt = \frac{1}{\lambda}$

System Reliability

System Reliability is a function of the interdependence of plant components as shown in Figure 7.

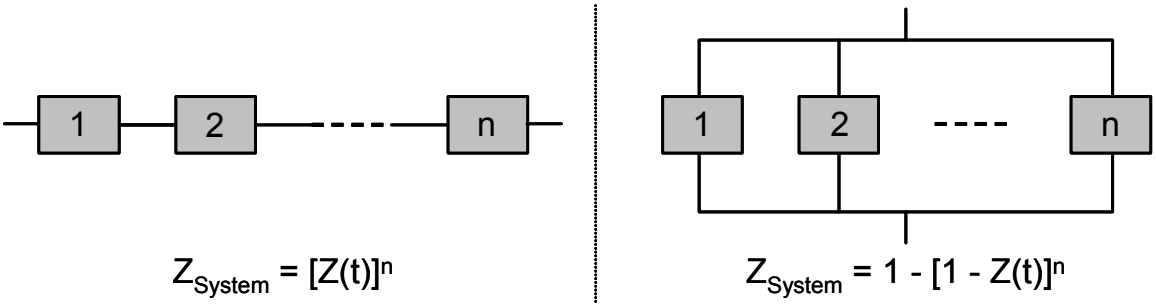

Figure 7. Possible System Structures.

The reliability of such a series system is the product of the reliability of the individual processes (subsystems):

$$Z_{System} = Z_1 \cdot Z_2 \cdot \ldots \cdot Z_n = \prod_{i=1}^{n} Z_i$$

The reliability of a parallel network containing redundant system components is given by:

$$Z_{System} = 1 - (1 - Z_1) \cdot (1 - Z_2) \cdot \ldots \cdot (1 - Z_n) = 1 - \prod_{i=1}^{n} (1 - Z_i)$$

A Markov model of randomly occurring failures was created. If *i* is the state of the system, then $P_i(t)$ is the probability that the system is in state *i*. Using the Markov approach, the system can be described by the following differential equations:

$$\dot{P}_0(t) + \lambda P_0(t) = \mu P_1(t)$$

$$\dot{P}_1(t) + \mu P_1(t) = \lambda P_0(t)$$

Assuming that at $P_0(t=0)=1$ and $P_1(t=0)=0$, the above equations can be solved to get:

$$A(t) = P_0(t) = \frac{\mu}{\lambda + \mu} + \frac{\lambda}{\lambda + \mu} \cdot e^{-(\lambda + \mu)t}$$

Figure 8 shows the resulting plant reliability for multiple plant design options, ranging from no redundancy (Blue solid line RA), to various partially redundant robot configurations (cases RB through RD), to a fully redundant plant (case RE), in which the tasks of a failed robot are immediately assumed by a parallel, redundant manipulator.

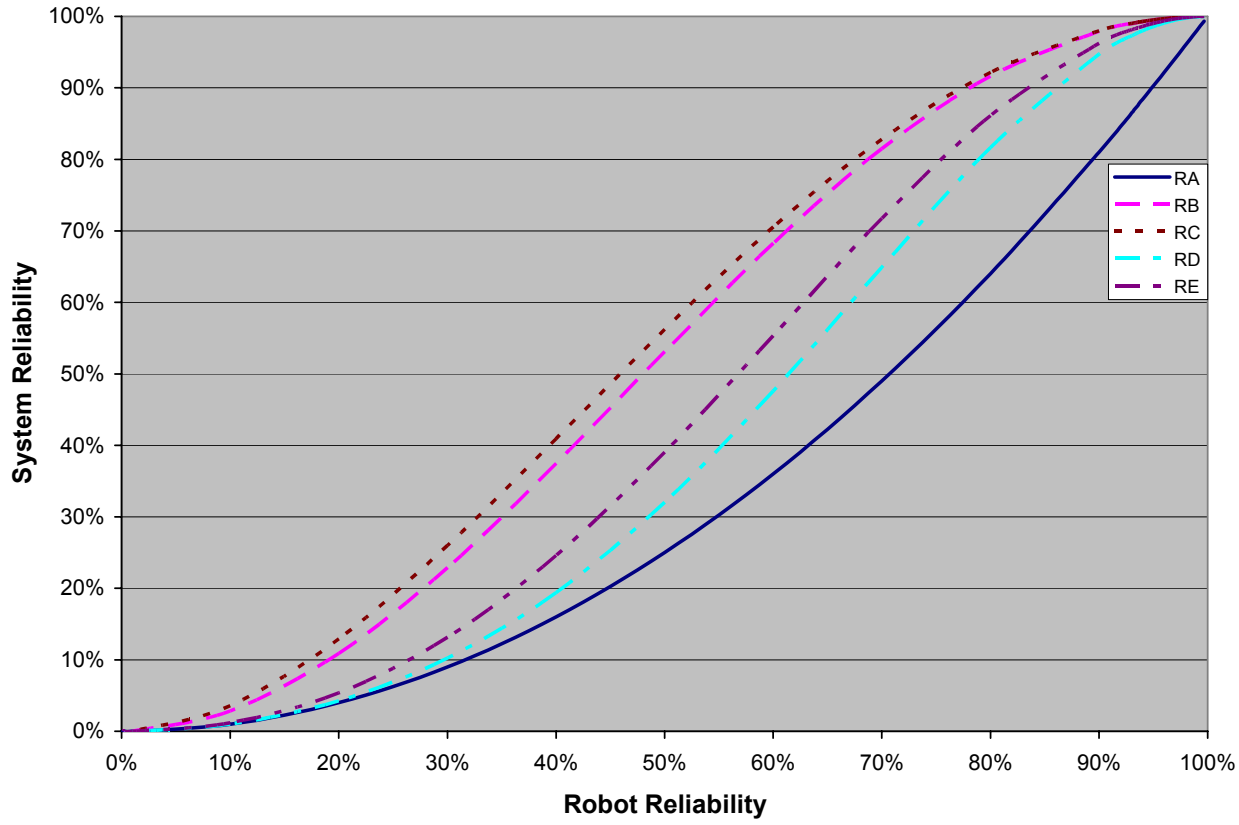

Figure 8. Reliability for multiple plant layouts as a function of robot redundancy.

Impact of the Synthesis Process on Structure Properties for AFCI Fuel Candidates (Task 28)

Transmutation-related research work at the national laboratories, e.g., Los Alamos National Laboratory, is focused on mono-nitride ceramic fuel forms, and consists of closely coordinated "hot" actinide and "cold" inert and surrogate fuels work. Matrix and surrogate materials work involves three major components: (1) fuel matrix synthesis and fabrication, (2) fuel performance, and (3) fuel materials modeling. The synthesis and fabrication component supports basic material studies, as well as actinide fuel fabrication work through fuel fabrication process development.

This task supports the program by delivering structural data on surrogate and radioactive fuels. Crystal structure and nanostructures of the individual fuel type, oxides and nitrides, as considered for GEN IV and HTR particle fuels are determined. Therefore, three different

approaches on fuel synthesis are applied: (1) dry chemical route, (2) wet chemical route, and (3) sol-gel microsphere pelletization (SGMP) process.

Ceramic Nitride Fuel in the System ZrN-ErN-UN

Sample Preparation

Radioactive nitride fuel samples were produced through carbothermic reduction / nitridization of phase-pure oxide solid solutions in the system ZrO_2-$ErO_{1.5}$-UO_2. For now, phase-pure mononitride fuels could not be synthesized and the content of mononitride was found to range from about 33 wt.-% to 67 wt.-% depending on sample and thermal treatment. In addition to the mononitride solid solution phase, a second fcc phase was identified which could represent either solid solution phase: (1) uranium dioxide-based or (2) uranium dinitride-based. Lattice parameter, space group, and calculated diffraction intensities are nearly identical for either eventual fcc-solid solution phase and their definite identification entirely by XRD/Rietveld analysis is not possible. Using EELS might be a reasonable approach for identifying this second phase and therefore electron transparent TEM samples had to be prepared. Different approaches were tested for TEM sample preparation on radioactive samples. Polishing - dimpling – ion-milling was found to be superior to low-angle-wedging – ion milling. Alternatively, a new procedure was developed on very brittle ceramic samples which might eventually be to fragile to survive standard sample preparation procedures. This category of samples could be prepared using the ultra-microtome after mixing ground sample powder with Spurr resin (Figure 9).

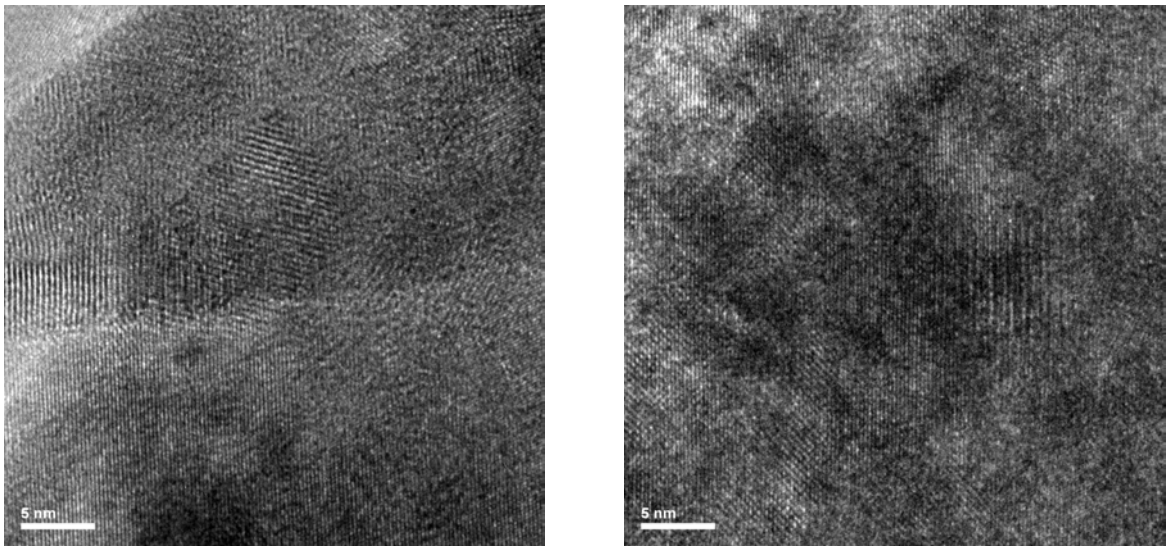

(a) *(b)*

Figure 9. High resolution image of radioactive ceramic nitride fuel after carbothermic reduction/nitridization of oxide solid solutions. (a) Interface between two solid solution phases. (b) secondary oxide/nitride solid solution phase. The radioactive ceramic TEM sample was prepared using an ultra-microtome. The images are 1,000,000 times magnified.

EELS Nano-Probing

The synthesis of radioactive nitride fuel in the system ZrN-ErN-UN through carbothermic reduction/nitridization led to the formation of a mononitride solid solution phase and an unidentified dioxide, or dinitride fcc solid solution phase. To clearly determine this second phase, electron energy-loss spectroscopy (EELS) was applied on an electron transparent radioactive sample prepared by dimpling and ion-milling.

The high resolution images exhibit the crystalline nature of the nitride solid solution fuel samples and the lattice fringes are resolved as shown in Figure 10. The TEM sample preparation procedure was optimized using dimpling and low-angle ion-milling. However, high resolution imaging did not allow one to clearly distinguish the two crystalline fcc-phases at hand.

At magnifications of about 100,000 times and applying STEM mode, the two fcc solid solution phases can be distinguished and analyzed by EELS as shown in Figure 11.

Based on EELS spectroscopy shown in Figure 12 it was not possible to clearly distinguish between nitride and oxide solid solution phases eventually present in the chemical system as investigated. Based on the published EELS data on UO_2 its presence in the sample could not be confirmed, and published data on ZrN and UN are not available. To overcome these shortcomings, one will have to synthesize reference material for the systems ZrN-ErN-UN and ZrO_2-$ErO_{1.5}$-UO_2 in order to maintain an in-house database on suitable EELS reference data.

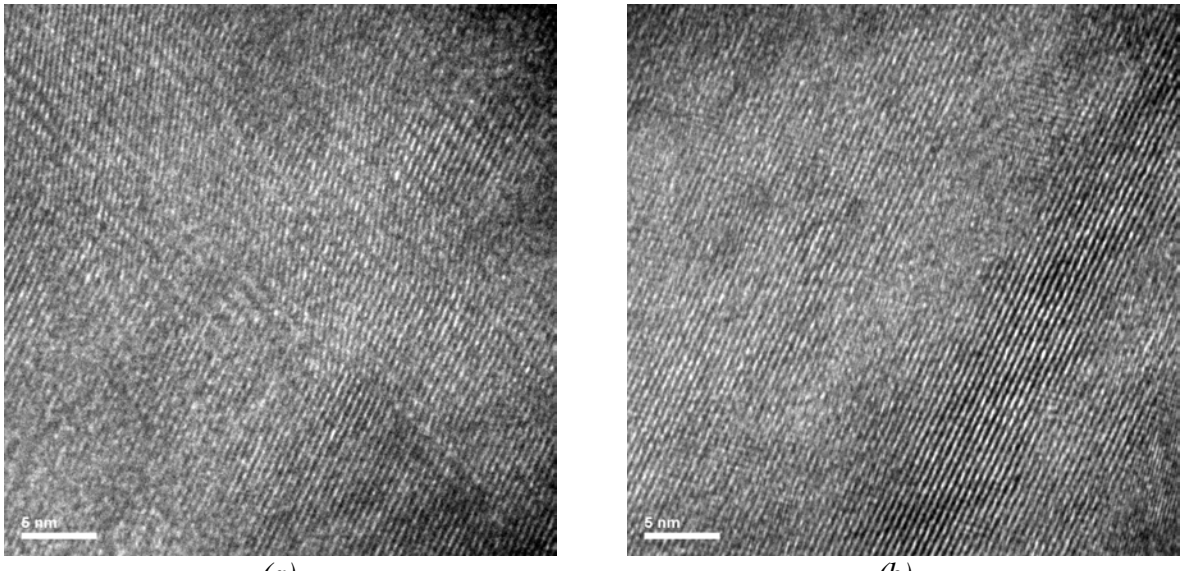

(a) *(b)*

Figure 10. High resolution image of radioactive ceramic nitride fuel. TEM sample was prepared using dimpling and ion-milling. The images are 1,000,000 times magnified.

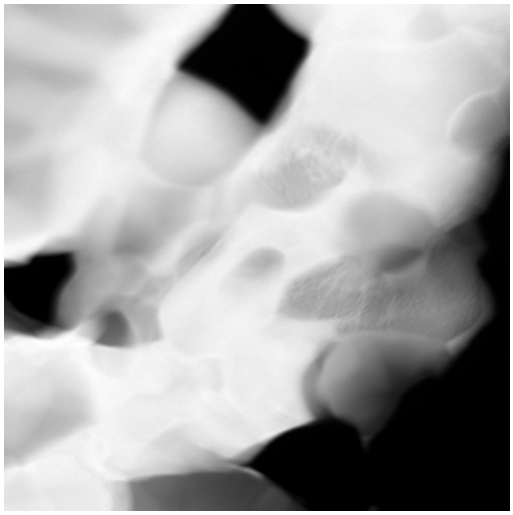

Figure 11. STEM image of ceramic nitride fuel 96,000 times magnified.

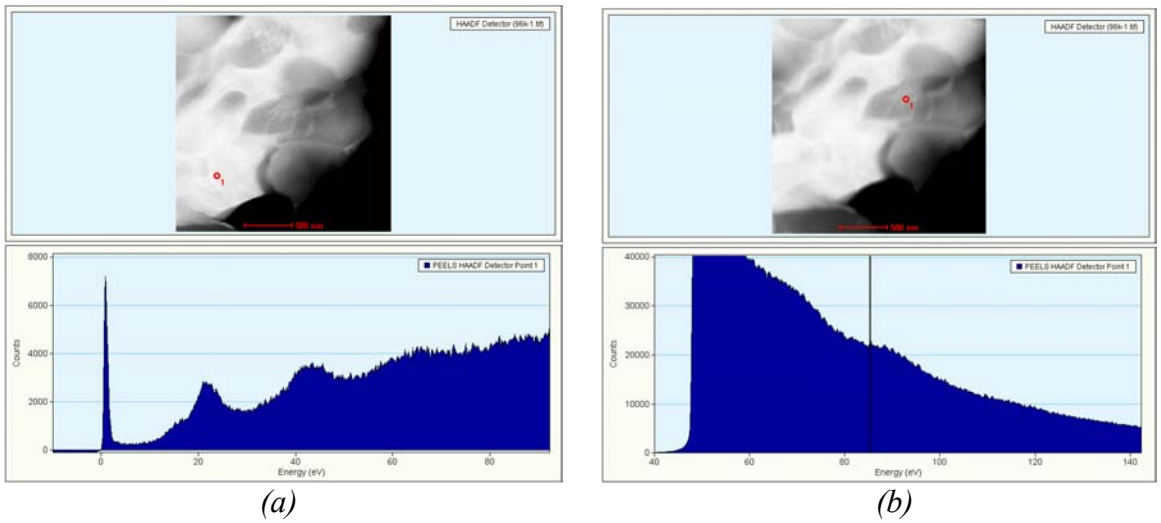

(a) *(b)*

Figure 12. EELS spectra of fcc-solid solution phases.

Thermal Analysis

Ceramic ZrN surrogate fuel samples (provided by LANL) were analyzed by TGA/DSC thermal analysis in the temperature range of 25°C to 1400°C in N_2 atmosphere, and changes in phase constitution and crystal structure were analyzed by XRD-Rietveld analysis and TEM. One of three ZrN samples exhibited an exothermal reaction at about 1169°C while all samples gain about 1% in weight associated with the formation of Zr_2ON_2 and increased cubic zirconia contents. To furthermore determine the impact of TGA/DSC heat treatment on the micro/nano structure of nitride fuel samples, a ZrN sample was analyzed before and after TGA/DSC by TEM (Figure 13).

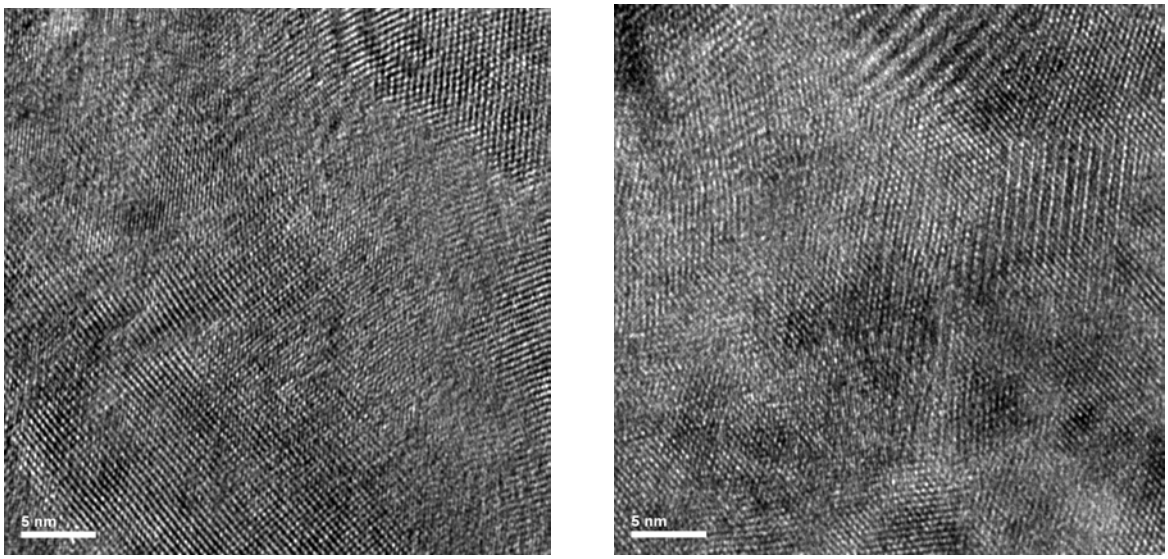

(a) *(b)*

Figure 13. ZrN sample before and after TGA/DSC thermal analysis.

Based on the TEM investigation it can be concluded that the nanostructure of ZrN is not affected by TGA/DSC thermal analysis. Before and after thermal analysis the ZrN nanostructure is characterized by 10 nm to 50 nm sized domains and a mosaic-type nanostructure is developed. However, the fitting of the Lorentzian XRD peak profiles and the calculation of the average crystal size based on the Scherrer equation indicates an increase in the average crystal size by the thermal treatment (25°C to 1400°C, 10 K/min, N_2 atmosphere) from about 125 nm to about 350 nm. As a conclusion, the phase formation of Zr_2ON_2 and the slightly increased cubic ZrO_2 content in TGA/DSC treated samples do not negatively affect the crystallinity of nitride ADS fuels and their physical properties will not deteriorate.

SEPARATIONS TECHNOLOGY

Immobilization of Fission Iodine (Task 15).

During the last quarter, exploration of the reduction of iodate using the leucocrystal violet method (LCV) previously reported was continued. Initial experiments were done at 0.2 mM iodate. For the hydroquinone experiments the reaction rate was fast enough at ~ room temperature for investigation by continuous spectrophotometry. Lignin appeared to be non-reactive under these conditions. However, by increasing the iodate concentration in solution the reduction reaction could be followed at lower temperature and was amendable to continuous spectrophotometric monitoring. Lignin concentrations about ~50 ppm were difficult to monitor by uv/vis spectrophotometry.

Results at 32^{o}C are shown in Figure 14 for several different alkali lignin concentrations. The reaction rate clearly depends on lignin concentration. The iodate concentration is approximately constant under these conditions, and the slowing of the reaction with reaction time is a reflection

of the heterogeneous nature of lignin, as less that 1% of the iodate has reacted during these experiments.

A plot of the natural logarithm of the initial reaction rate against the natural logarithm of the alkali lignin concentration is shown in Figure 15. To a reasonable approximation the reaction is first order in lignin. The units of the rate constant are in ABS (592) units/ sec.

The temperature response for the reaction was also measured using this method as shown in Figure 16. The cuvette (reaction cell) temperature was adjusted by circulation water from a controlled temperature bath through the base of the cuvette holder. Temperature was monitored with a digital thermometer. The apparent activation energy for the reduction of iodate is 54.6 kJ/mol.

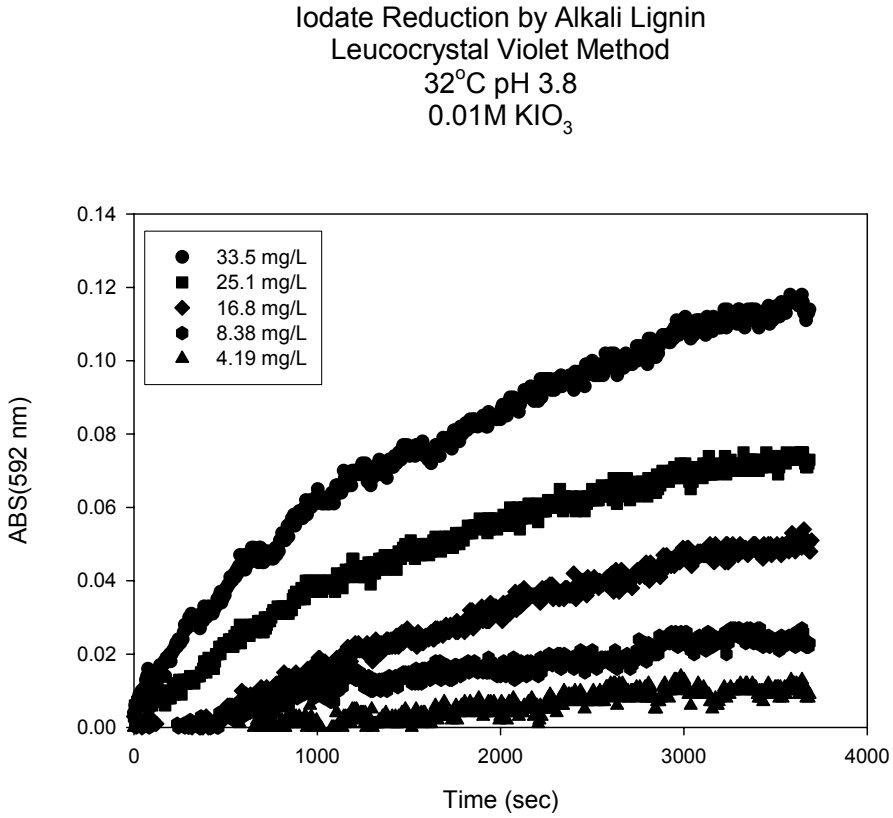

Figure 14. Reduction of iodate by alkali lignin at 32°C and pH 3.8. The intermediate IOH or I_2 oxidizes leucocrystal violet to crystal violet.

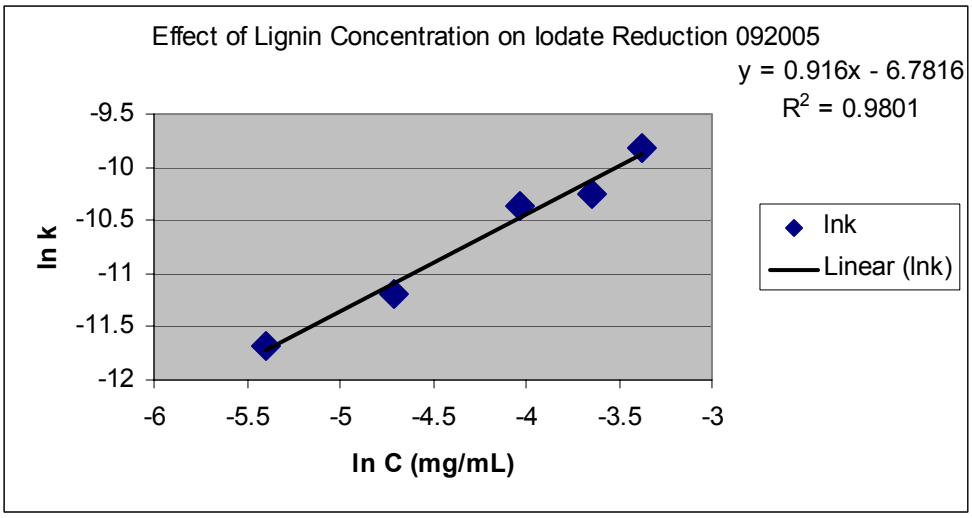

Figure 15. The effect of lignin concentration on the pseudo first order reaction rate. To a good approximation the reaction is first order in NOM.

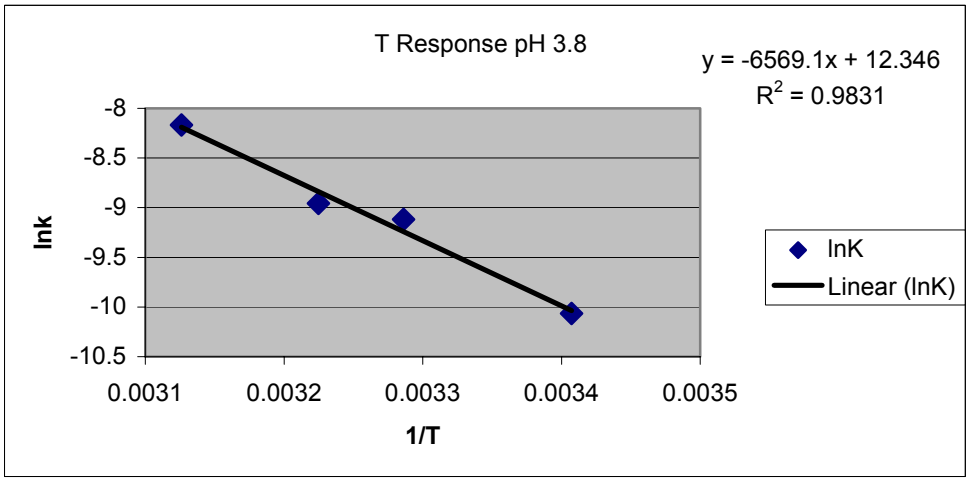

Figure 16. The iodate reduction reaction has an Arrhenius like behavior.

Earlier in this program it was found that a large fraction of iodine associated with natural organic matter (NOM) could be released during pyrolysis as methyl iodide. This methyl iodide should be recoverable for conversion to a transmutation target. At present, sodium iodide has been proposed as a viable transmutation target. Therefore a main priority was to develop a procedure for converting methyl iodide to sodium iodide. During this last quarter this conversion was attempted using the Würst reaction. In this procedure, metallic sodium would react with methyl iodide to produce sodium iodide and ethane. The reaction was attempted in several solvents without success. The sodium napthalide was also attempted as a reductant without success. An alternative method was to investigate decomposition by hydrolysis or another nucleophile as a means of obtaining sodium iodide from methyl iodide.

In order to follow the decomposition of methyl iodide all reactions were performed in 65 mL partially filled (10 mL) septum sealed bottles. The vapor phase above the bottle was sampled (0.1 mL) with time and methyl iodide was monitored by GC/MS. Using this method an attempt was made to react methyl iodide with sodium hydroxide (at several different temperature and concentrations of sodium hydroxide). As confirmed in the literature, the reaction rate is very slow. The potential of several other nucleophiles were then investigated.

Reasonable conversion rates were obtained using thiourea and mercaptoethanol (results are not shown). These nucleophillic reagents react with methyl iodide producing HI and a methylated nucleophile, requiring cation exchange chromatography to convert the HI to NaI. Also investigated was the ion exchange resins that contain mercaptan (-SH) functionalities. GT-73 is a commercially available resin that contains $–CH_2SH$ groups bound to a polystyrene matrix. The reaction of methyl iodide with the resin would produce $–CH_2S\text{-}CH_3$ and HI. The HI produced can be titrated with NaOH. As expected, it was found that adding NaOH to the reaction mixture substantially increases the reaction rate of methyl iodide with the resin. The NaOH deprotonates the mercaptan producing a more aggressive nucleophile and produces NaI as a product. An example of this reaction is shown in the Figure 17. This reaction was performed in 0.2 M NaOH (10 mL) in the presence of 1.0 g of GT-73 (damp resin as received). The methyl iodide concentration was 8.1 mM. The same reaction was performed in a 50% methanol solution and was essentially complete after 2.5 hours. The presence of methanol apparently enhances the reaction of methyl iodide with GT-73. Iodide formation was verified using the ion selective electrode method described in a previous report.

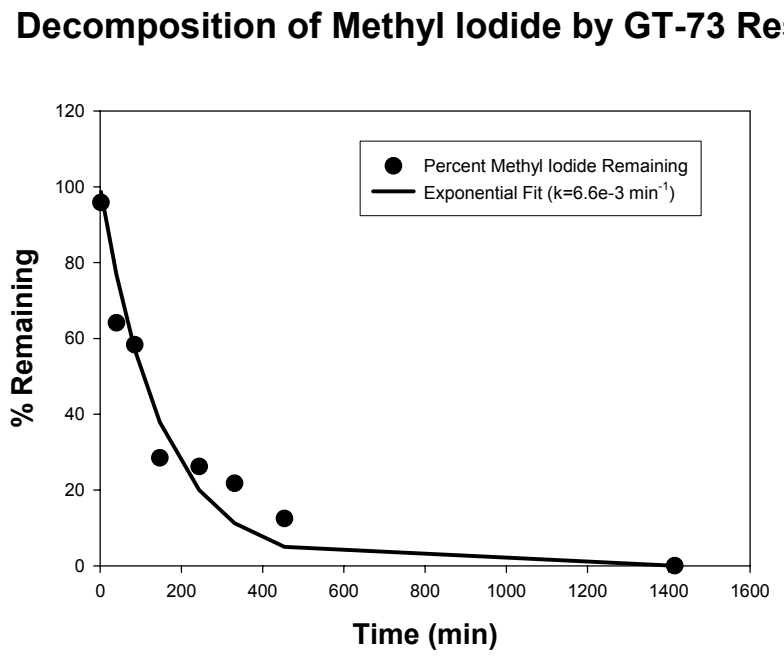

Figure 17. The decomposition of methyl iodide by GT-73 resin (1 gram in 10 mL) in 0.2 M NaOH.

Additional experiments were continued with the preparative gas chromatograph described in a previous report. The packed column gas chromatograph is an SRI 8010 with a TCD detector and injector valve equipped with a thermal desorber. The thermal desorber has a trap packed with carbosieve. Volatile materials that are collected on the carbosieve trap can be transferred to the gas chromatograph by actuating the valve and activating the thermal desorption oven. In order to scale up the pyrolysis experiments, a 6" tube furnace manufactured by Carbolyte was used. This programmable furnace has a 0.5" diameter process tube that can hold 8-200 mg samples of NOM. The furnace is connected to a source of helium with Swagelok™ fittings. During sample heating, helium sweeps products from the tube furnace to the carbosieve trap located in the thermal desorber unit. Chromatography is initiated by thermally desorbing trapped volatiles from the carbosieve trap to the GC column (2mm x 2m, Porapak Q). The instrument was calibrated by injecting methyl iodide into the thermal desorber trap. The response factor and retention time of methyl iodide were thus determined. During this quarter it was ascertained that methyl iodide eluting from this GC could be collected in an impinger containing 5.0 mL of methanol. The methanol was transferred to 65 mL septum sealed bottles diluted with water (50%) and analyzed the headspace analyzed by GC/MS. Using this technique it was demonstrated quantitative recovery of methyl iodide. The retention time of methyl iodide was ascertained by running standards under the same conditions. These standards were used to establish "collection" times for methyl iodide produced by pyrolysis.

In order to demonstrate that methyl iodide could be recovered from NOM, iodinated samples of alkali lignin, sphagnum and an organic soil (Pahokee peat) were prepared. Previous results indicated that low pH promoted the reduction of iodate; therefore 1.0 g of each NOM sample was allowed to react at room temperature with 50 mL of 0.01M KIO_3. The pH was ~2 (1% phosphoric acid). After the reaction period iodate and iodide were quantified. Organic iodine was calculated by difference. The NOM was recovered from the suspensions by either centrifugation (alkali lignin and Pahokee Peat) or vacuum filtration (sphagnum) and dried for 48 hours in a vacuum desiccator over NaOH pellets. The organic matter was then pyrolyzed (0.05 – 0.1 gram) in the tube furnace and methyl iodide collected and quantified as described above.

An example chromatogram, recorded as a Thermal Conductivity Detector (TCD) response, is shown below in Figure 18. The large methyl iodide peak was collected and GC/MS analysis demonstrated that it was >95% methyl iodide.

The results from the three NOM samples are summarized in Figure 19. The alkali lignin removed all of the iodate from solution. About 35% of this iodate was reduced to iodide. The sphagnum peat removed about 80% of the iodate. From mass balance all of the iodate that reacted remained associated with the peat as organic iodine. The Pahokee peat proved the least reactive with only about 15% of the iodate removed during this reaction period. Iodide was not produced by the reaction of the Pahokee peat. Pyrolysis results indicate that 50 to 80% of the organic iodine was converted to methyl iodide and recovered by this procedure.

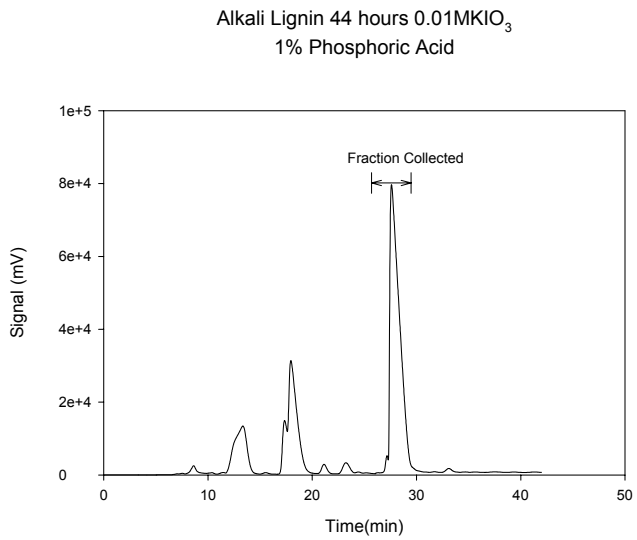

Figure 18. An example chromatogram from pyrolysis of 0.05 g of iodinated alkali lignin at 400°C. The methyl iodide peak collected is indicated.

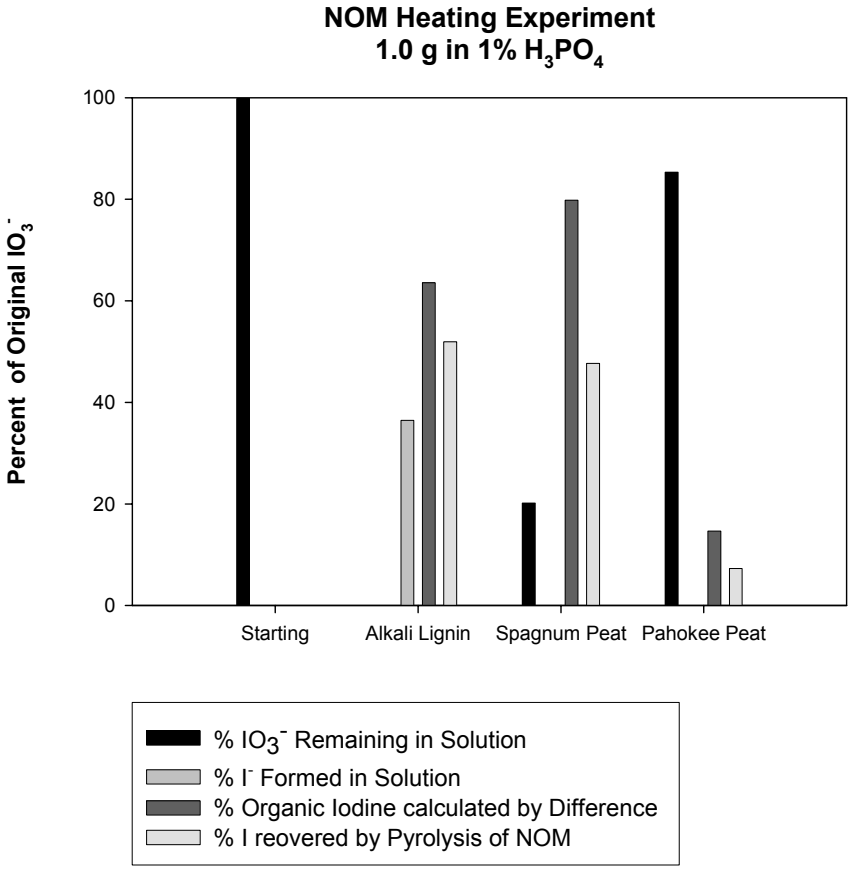

Figure 19. Distribution of iodine after iodate-NOM experiments at room temperature and pH 2. The initial iodate concentration was 0.01 M. The organic iodide was calculated by mass balance. The recovered iodine (as methyl iodide) is also shown.

Development of Integrated Process Simulation System Model for Spent Fuel Treatment Facility Design (Task 24).

Refinement of the TRPSEMPro Software Package

The intention of developing TRPSEMPro software was to accelerate research progress and to efficiently analyze research results. The implementation of database system was completed. Upon the request from ANL, more research notes and details need to be included into each flowsheet simulation run. More information can be further documented into the database for later validation and progress tracking. The improvement for this quarter was to complete such interface. Currently the description field shown in Figure 20 can take more information from the user and save into database.

The analysis result query process takes time to complete. A progress indication was implemented. Figure 21 shows the process window while doing the simulation.

Although several data sufficiency validation processes were performed internally in the previous TRPSEMPro version, the user is still required to check data entry and validation manually. The newly implemented function visually indicates the data validation results with the display of color-coded boxes. Boxes will be colored as light Green while all information is correctly entered as shown in Figure 22a. Figure 22b shows the missing data scenario with boxes coded red.

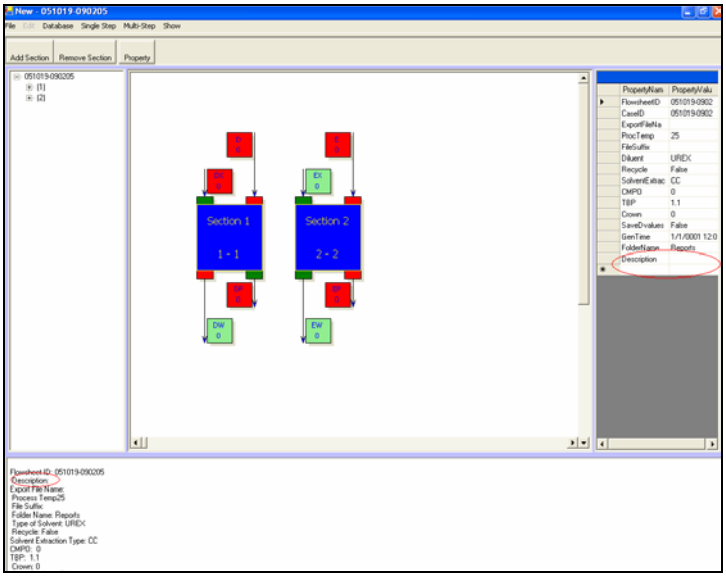

Figure 20. Searchable documentation feature can be located under "Description" field for each flowsheet simulation.

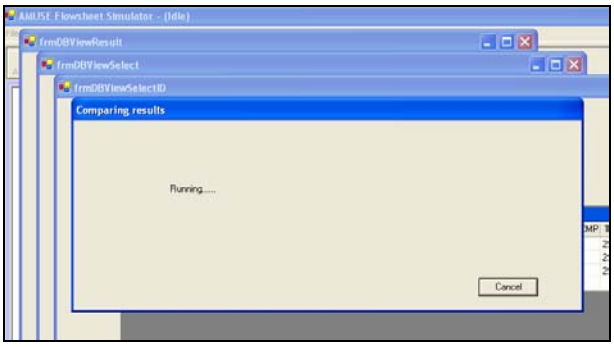

Figure 21. Message box indicates the "Simulation is in Progress".

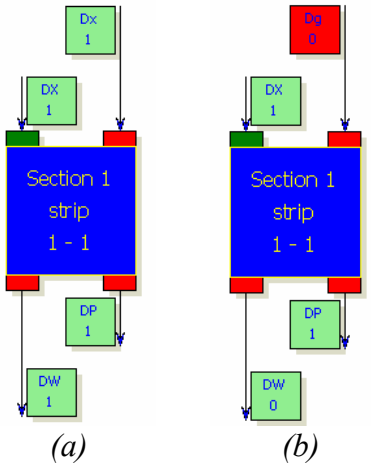

Figure 22. (a) The data entry is completed with all boxes coded light green, (b) the flow rate is missing with the top box coded red.

Construction of ASPEN-plus Separation Flowsheets

Separation of Acid – According to the requirement from ANL, simulation of separation of acetic acid and nitric acid (aqueous solutions) are needed. The objective is to study the effects due to the nitric acid molarity increasing. For the process, a distillation column is selected to separate the species based on relative volatilities. Figure 23 shows the simplified process.

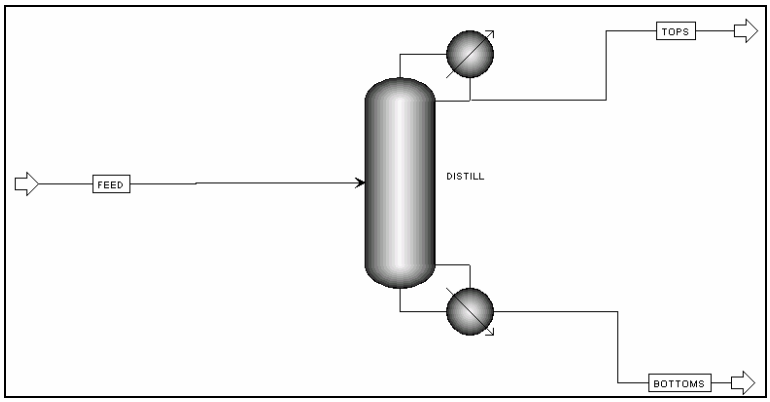

Figure 23. A separation process using acetic acid/nitric acid.

As given by ANL researchers, as shown in Figure 24, 4 unit operations convert Pu-HNO_3 to PuF_4. These four operations will be simulated as three processes in ASPEN Plus. The final unit operation of oxalate removal by a doctor blade cannot be simulated in ASPEN plus. This process is used to grind up the finished product and does change the chemical composition of the desired product. ANL is interested in simulation of chemical changes and not necessarily introducing size variation.

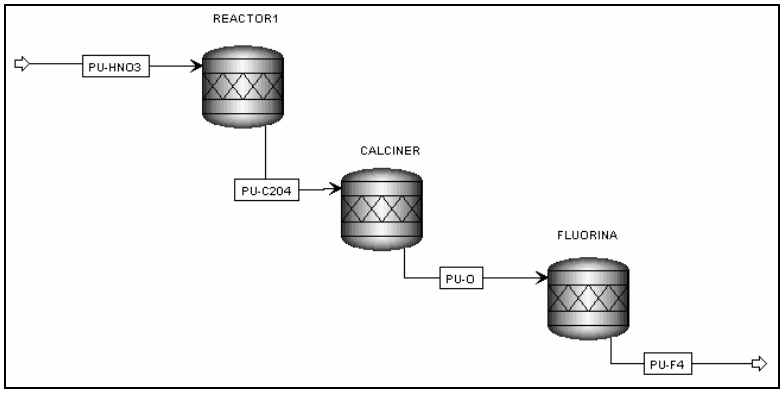

Figure 24. Pu separation process.

With respect to the Pu separation, the ASPEN Plus component bank does not have plutonium tetra fluoride. This data has to be added by the user. The chemical data is needed for this compound.

Electrochemical Separation of Curium and Americium (Task 25).

This research report outlines the current status and progress associated with the electrochemical separation of Curium and Americium. The following pages outline the progress on the project to date. Research has been actively perfomed on this project for 15 months and are currently on schedule for the proposed timelines. The last quarter has been extremely productive. The complexation and electrochemical measurement of EDTA has been accomplished to expand the

ability to measure the redox behavior of the species in pH regions that typically would cause precipitation. The electrochemical response of Ce at a Pt electrode after complexation with EDTA is presented in Figure 25.

The data in Figure 25 show that the complex is stable at pH values much higher than required for the precipitation of $Ce(OH)_x$ (s). The highest stability is observed at pH = 6 indicative of the largest current response. The data suggests that complexation can be used to make species stable in pH regimes that are typically unfavorable.

Using this knowledge, the complexation of Ce in polymeric membranes will be examined. The first step involves the synthesis of the polymer membrane. This is followed by the reduction of Au particles in the polymer membrane to produce a conductive polymer/metal composite. Attaching chelating agents to the gold surfaces embedded in the polymer ensures that the chelation species in the membrane does not leach to the solution. The first two steps have been completed and have confirmed the presences of Au in the polymer membrane. Figure 26 shows the SEM images of the polymer prior to and after incorporation of the Au.

The ligand has been prepared in small quantities for the initial studies with the PANI/Au composite. The ligand is a disulfide derivative of EDTA providing to thiol linkages to anchor the species in the membrane as shown in Figure 27.

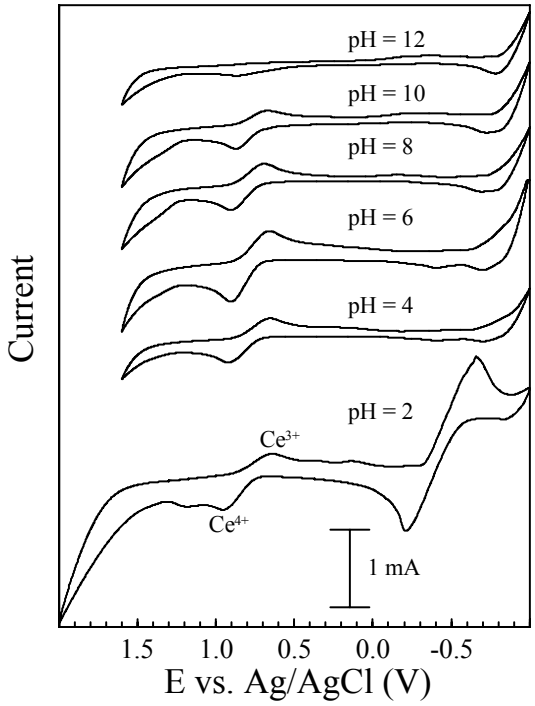

Figure 25. Electrochemical response of Ce/EDTA complex as a function of pH.

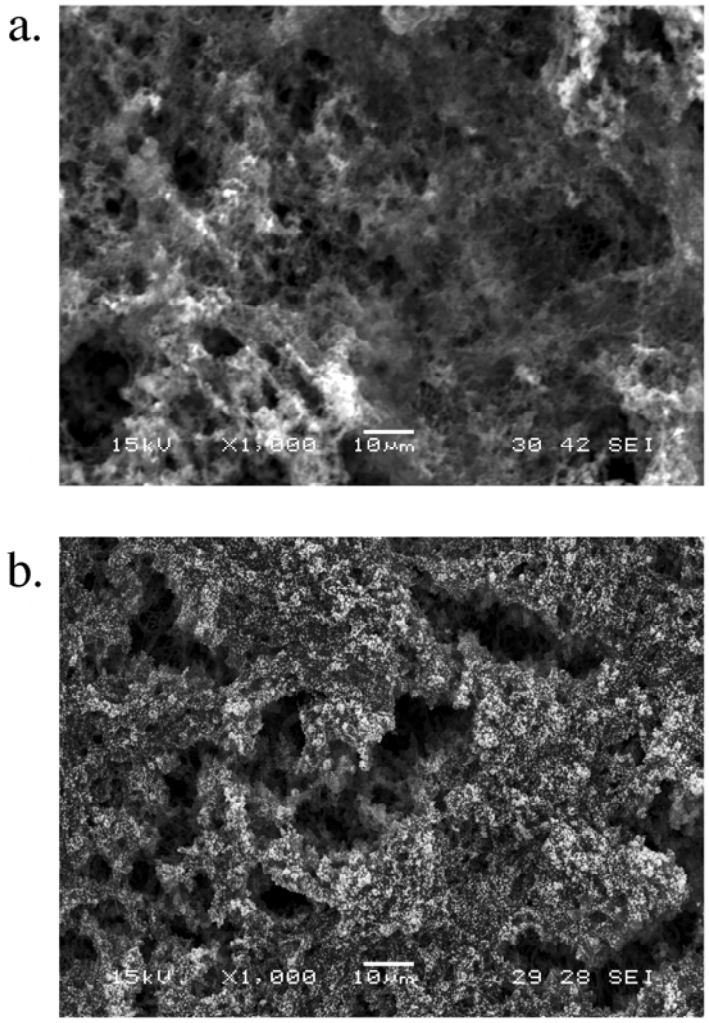

Figure 26. SEM of (a) Polyaniline (PANI) and (b) PANI/Au.

These linkages will be exploited to provide the separation of similar solution species. The first step is characterization chelation of a variety of species to ensure the potential for the processes are significantly different. In this manner the potential can be used to control for the separation of two similar species using the polymer membranes.

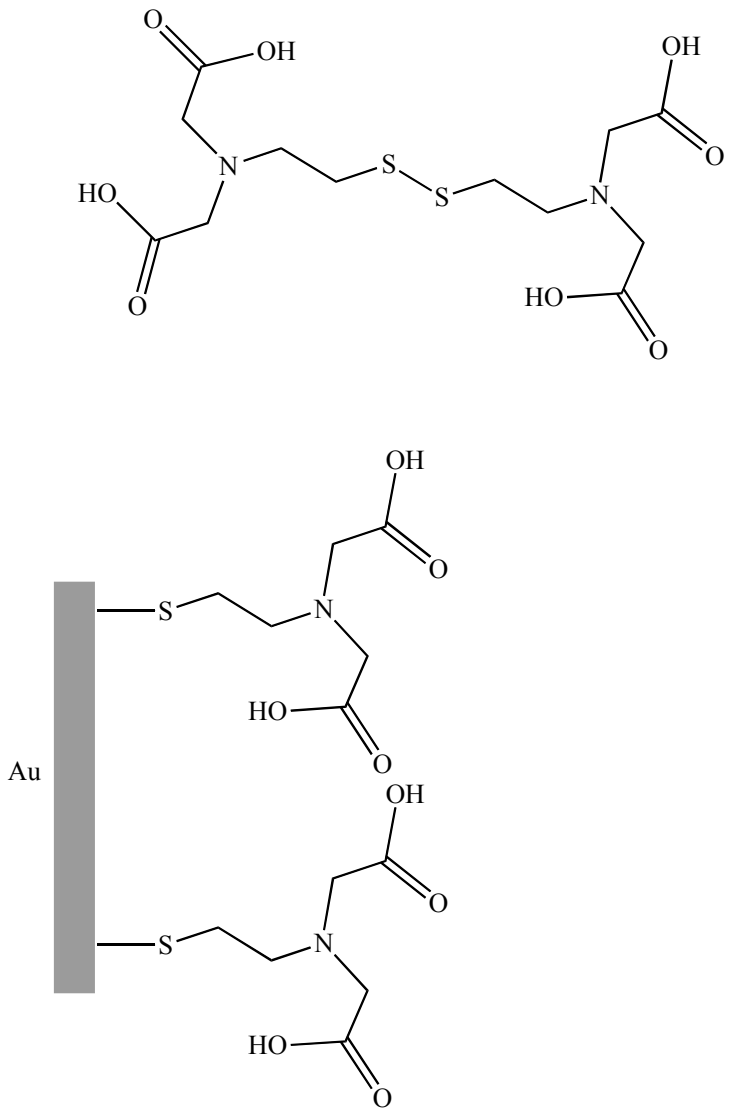

Figure 27. A ligand that is a disulfide derivative of EDTA providing thiol linkages to anchor the species in the membrane.

Fundamental Chemistry of U and Pu in the TBP-Dodecane-Nitric Acid System (Task 26).

Nitrate Determination

For most of this quarter HPLC was used to measure nitrate. Many experiments were run in order to determine the precision, accuracy, and the reliability of the instrument. This was also used to measure a second batch of pre-equilibrated samples. It was used to measure both the aqueous and organic portions. These experiments did prove to be successful. The only problem was the fact that troubleshooting was usually required in order to get the HPLC operational before each use. This was very time consuming. This seemed to be the best method, until the use of IC was made available. This instrument is much newer and more reliable.

This instrument is actually two ICs in one. It has a Dionex ICS 2000 for measuring cations, and a Dionex ICS 2500 for the anions. It has an autosampler and dual injection system in order to run both at the same time. The 2000 is able to measure Li^+, Na^+, Ca^{2+}, K^+, and Mg^{2+}. The 2500 can measure F^-, Cl^-, NO_2^-, SO_4^{2-}, Br^-, NO_3^-, PO_4^{3-}. Both have conductivity suppressors which the samples go through before reaching the detectors. There are both conductivity and UV detectors available to use with this instrument. As for the determination of nitrate, the method used is very similar to the one used with HPLC. The same dionex anion exchange column is used with the same 30μM KOH elugen solution. The IC can also be used to measure both aqueous and organic samples. The instrument software is newer and more user friendly. Another plus for the IC is the fact that it can be used to measure lithium as well as nitrate. Also the measurement of nitrite could aid in the understanding of the degradation of nitrate. Overall, it now seems that IC is the better method of nitrate determination.

This method was used to measure the pre-equilibrated samples with results comparable to the HPLC. The data shows that in the absence of uranium the distribution of nitrate into the organic phase increases and reaches a plateau as nitric acid and total nitrate increase. There is an increase in the amount of nitrate in the organic phase as the nitric acid concentration increases. Also within a given acid concentration the amount of nitrate extracted in the organic phase increases with increasing total nitrate concentration. This data is shown in Figure 28.

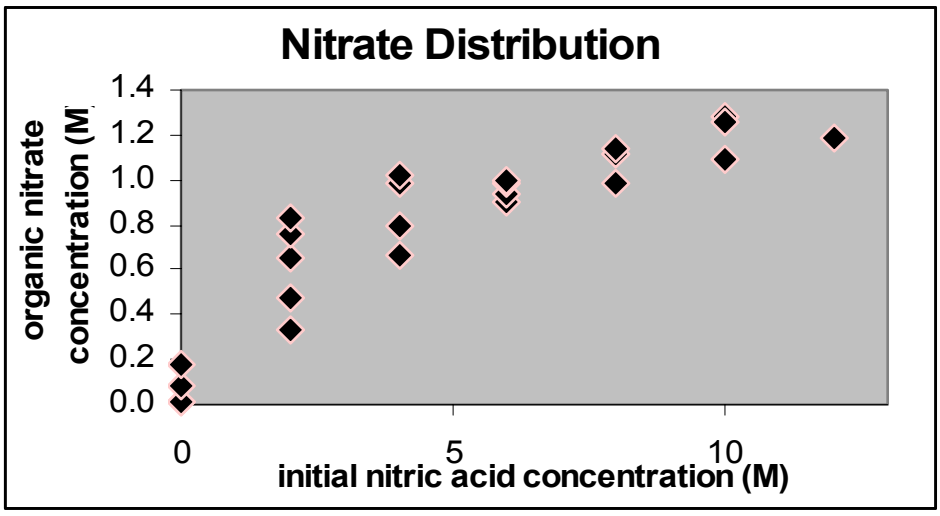

Figure 28. The amount of nitrate extracted in the organic phase within a given acid concentration.

HPLC (high performance liquid chromatography) has been shown to be the best way measure the nitrate concentration in the extraction samples. The HPLC measurements are not affected by the acid concentration, unlike measurements with a nitrate specific electrode. Another advantage is the fact that the HPLC can measure organic samples directly. The method used will consist of a dionex anion exchange column with a column guard. The eluent used is a 30 mM KOH solution. This gives a nitrate peak at a retention time of about 8.3 minutes. The linear range is very large; ranging from 0.01 to 500 ppm. The samples from the uranyl-TBP studies will be

diluted to fit into the calibration range of 0.1 to 100 ppm. This method has been successfully used to measure the pre-equilibrated samples. The organic phases and standards are diluted in MeOH instead of water.

The titrator that will be used to measure acid concentration was sent in to the company for repairs, and an autosampler was purchased for this instrument. It should be operational in January. Also a new NMR is on the way which will be used to determine chemical structure around phosphorus in the TBP. This instrument should be operational by February.

XAFS Spectroscopy

Different hypotheses were proposed in the literature concerning the nature of the U species in the heavy organic phase in:

(i) formation of the compound $HUO_2(NO_3)_3.xTBP$ (Solovkin et al., "Formation of a third phase in the system $UO_2(NO_3)2HNO_3$-H_2O-tributyl phosphate-kerosine," *Zhurnal Neorganicheskoi Khimii*, 1960, 5 2115-18)

(ii) formation of U(VI) polymer (Nemodruk et al., "Formation of polymeric compounds with uranyl nitrate in tributyl phosphate extracts," *Radiokhimiya*, 1969, 11(2), 229-32)

(iii) modification of nitrate bounding and formation of hydrogen bond with water or acid nitric present in the third phase (Chiarizia et al., "Third Phase Formation Revisited: The U(VI), HNO_3 - TBP, *n*-Dodecane," *System Littrell Solvent Extr. and Ion Exch*., 21 (1), 1-27, 2003)

According to EXAFS result obtained in this study the following was found for the different theories.

The hypothesis (i) is rejected since the formation of an eventual $HUO_2(NO_3)_3.xTBP$ will lead 6 O(N) atom at 2.50 Å and this was not found. As for hypothesis (ii), the simulation of EXAFS spectra of theoretical U(VI) dimer was performed and compared to experimental EXAFS spectra of heavy phase. During extraction of U(VI) by TBP, the formation of a dimer with a core structure $-[O=U=O-UO_2]^{4+}$ has already been suggested. This dimer results from the dimerisation of $UO_2(NO_3)_2.2TBP$ and $UO_2(NO_3)_2.TBP$ and is formulated $U_2O_4(NO_3)_4.3TBP$. The simulation of the EXAFS spectra of $[UO_2(NO_3)_2.2TBP]_2$ was performed in the k range [3 $Å^{-1}$, 13 $Å^{-1}$]. The simulation was performed in 3 steps:

1. Using the structure of $UO_2(NO_3)_2.2TBP$ and adding 1 U atom at 4.04 Å, the atomic position in the theoretical U_b-O=$U_aO(NO_3)_2.2TBP$ were calculated. This structure was used to simulate the EXAFS spectra (**χ1)** of the U_a atom in coordination 8.
2. Using the structure of $UO_2(NO_3)_2.2TBP$ and adding 1 O atom at 2.30 Å and 1 U at 4.04 Å, the atomic position in the theoretical U_a-O-$U_bO_2(NO_3)_2.2TBP$ were calculated. This structure was used to simulate the EXAFS spectra (**χ2)** of the U_b atoms in coordination 9.
3. The total EXAFS spectrum is the average of the **χ1 and χ2** spectra**.** The FT of the simulated EXAFS spectra of $[UO_2(NO_3)_2.2TBP]_2$ is presented in below, this simulated FT is compared to the U15 experimental one (heavy phase).

The structural parameters used for this simulation were those previously determined for U15 compound. A value of 0.008 was assigned to σ^2 for the single scattering U-U and to the multi

scattering U-O-U and 0.006 for U-O_{eq} scattering. Figure 29 shows that the simulated FT and the U15 FT are nearly identical between1 Å and 3.5 Å. The difference arise on the last peak at 4 Å, the peak of the dimer is larger.

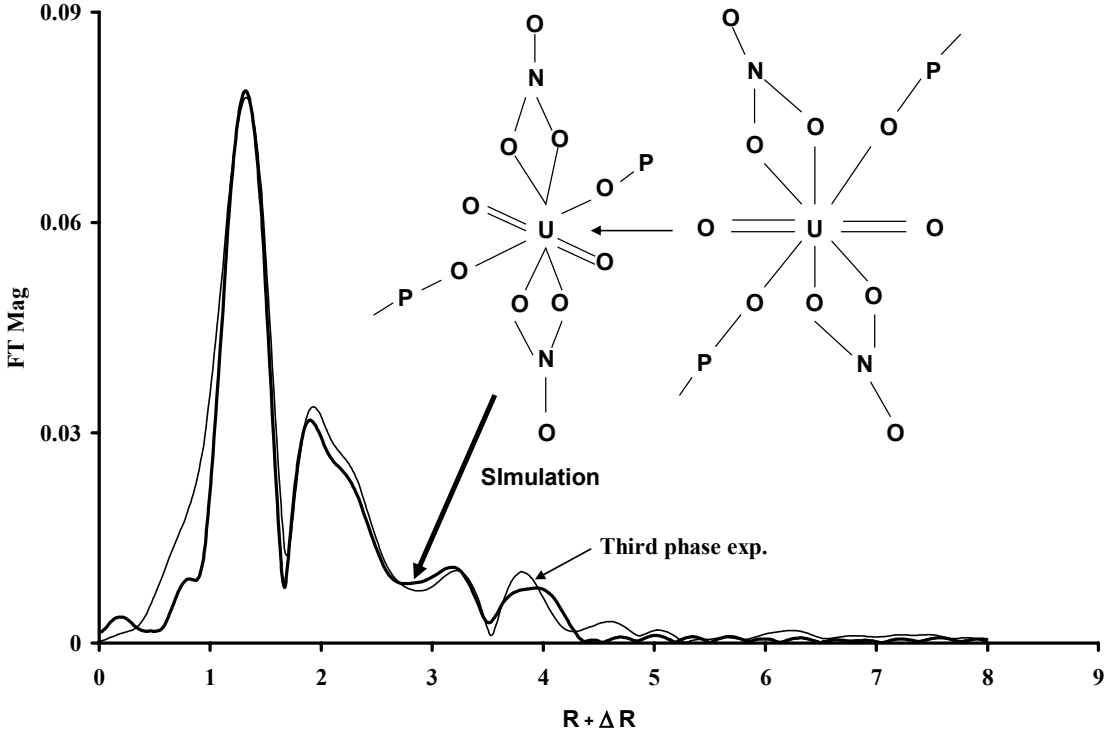

Figure 29. Structural parameters used for the simulation.

Since in $UO_2(NO_3)_2.2TBP$ and in the theoretical $[UO_2(NO_3)_2.2TBP]_2$ the environment around the U(VI) atoms is nearly identical, their EXAFS spectra must be similar, only a difference at long distance could be observed, nevertheless the intensity at 4 Å would not be very different. For this reason hypothesis (ii) cannot be completely rejected, and it might be possible that $[UO_2(NO_3)_2.2TBP]_2$ and $UO_2(NO_3)_2.2TBP$ are simultaneously extracted.

Hypothesis (iii) corroborates the observation done in 15 M HNO_3 media but is not verified in 8M and 12 M HNO_3 media. In 8 M and 12 M media, in the light and heavy phase, EXAFS measurements show that the environment around UO_2^{2+} is the same and constituted by 2 NO_3 and 2 TBP groups. When $[HNO_3]$ increases to 15 M, the number of oxygen atoms from bidentate nitrate decreases by 50%. This phenomenon has been explained by the change conformation of nitrate from monodendate to bidentate.

Considering an environment of bidentate and monodendate nitrate around UO_2^{2+}, the adjustment gives a value of 0.5 monodentate and 1.12 bidentate nitrates. Then, it might be possible that the heavy phase is a mix of U species which present different coordination mode of nitrate

Investigation of Optical Spectroscopy Techniques for On-Line Materials Accountability in the Solvent Extraction Process (Task 29).

Laser Spectroscopy Laboratory

The laser system was acquired and initial shakedowns are in progress. Initial calibration of the spectrometer started. The final pieces of safety equipment were ordered and shipped. The electrical refit of the laboratory was completed save for emergency "panic" button installation. Power throughput issues are being resolved in order to control for variation in the power delivered. The training program for the rest of the group was initiated.

UV/Visible Spectroscopy of Uranium

Work continued on the aqueous uranyl system. Preliminary data regression was matched to suspected speciation of uranyl ion in solution. Change in speciation seems to correlate to an increase in signal (Figure 30). An experiment is being designed to elucidate the exact nature of the dependence to attempt to separate the spectra of the mono- and di-nitrato species. Nitrate concentration appears to have a minimal impact on uranium detection limits. Further investigation is required to determine if spectral shifts are significant enough to allow determination of nitrate concentration directly from uranyl nitrate peaks.

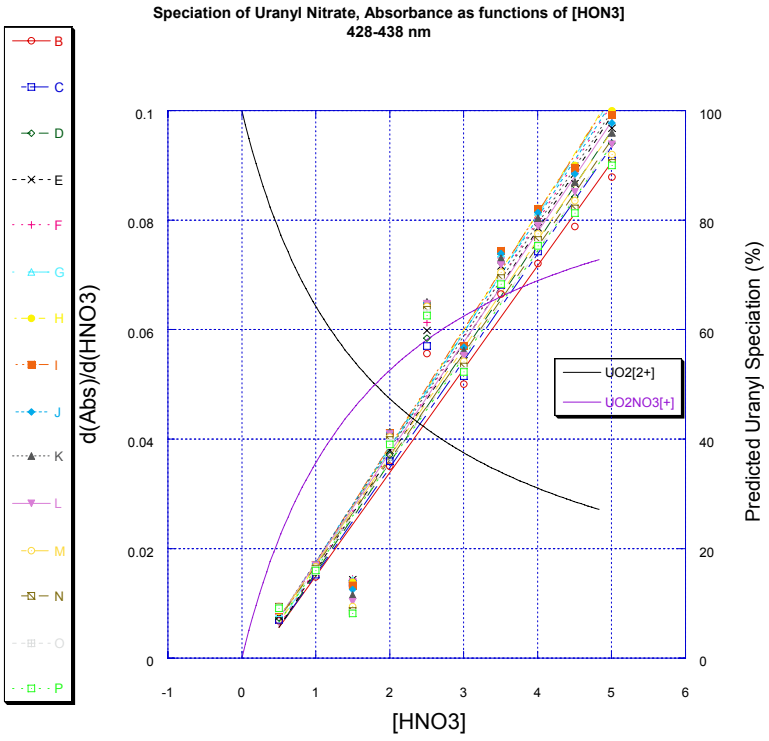

Figure 30. Speciation of Uranyl Nitrate.

Combined Radiation Detection Methods for Assay of Higher Actinides in Separation Processes (Task 30).

Monitoring of higher actinides (HA – includes neptunium, plutonium, americium, and curium) during the separation of used nuclear fuel has been identified as a critical research area in the U.S. Advanced Fuel Cycle Initiative (AFCI). Recycling of used fuel by chemically separating it into uranium, fission products, and HA would be the first step in this new fuel cycle. Material Protection, Accounting, and Control (MPAC) is necessary for materials accounting, criticality monitoring, and assurance of proliferation resistance. The objective of this MPAC project is to develop technology to detect and accurately measure quantities of higher actinides in used fuel assemblies and processing systems without taking frequent samples. Process systems may include separations batches, pipelines, storage tanks, and fuel fabrication equipment. A variety of measurements may be combined to calculate flow rates of actinide elements with a to-be-determined precision.

In this project, faculty and students are investigating the potential to use combined neutron and gamma-ray detector systems to measure quantities and isotopic constituents contained during separations and intermediate storage. This will require knowledge of the nuclear and decay characteristics of materials during processing, the development of conceptual designs of monitoring systems, radiation transport studies to develop an understanding of operational regimes, and experiments to confirm performance. In addition, both passive and active concepts will be investigated, including collaborations with the Idaho Accelerator Center (IAC) at Idaho State University (ISU) to use electron linacs for producing photoneutrons in situ, for photon activation of HA, or for stimulating emissions processes (e.g. x-ray fluorescence).

The PI met with group leaders and technical staff at LANL in conjunction with the MPAC PI and others from Idaho State University to develop collaborations for monitoring systems development. The group met with the N-1 Safeguards Science & Technology Group and the N-2 Advanced Nuclear Technology Group. LANL visits to UNLV and ISU were scheduled for January and February.

As part of UNLV Task 6, assembly and programming of a new data acquisition system (DAQS) for the ^{3}He Neutron Multiplicity Detector System (NMDS) was completed and additional components were ordered. The DAQS was programmed and the detectors were re-assembled in a new detection laboratory space at UNLV after receipt of a new PC to support the new DAQS and analysis software. The NMDS was tested both with cosmic radiation (background counting) and with a weak ^{252}Cf source; results compared favorably with previous counting data.

In addition, students resumed developing concepts for combined neutron-gamma and passive-active interrogation systems using the NMDS. The NMDS will be used in Task 27 henceforth.

TRANSMUTATION SCIENCES

Neutron Multiplicity Measurements of Target/Blanket Materials (Task 6).

The previous quarterly report detailed how a new data acquisition system (DAQS) with a multi-component digital input/output board (Figure 31) was configured using an electronics lab personal computer. This system, which was developed to support higher count-rate experiments, uses LabView® software and was interfaced with the Neutron Multiplicity Detector System (NMDS). During the current reporting period, despite limited student time to work with the NMDS, a high-speed personal computer was purchased to host the data acquisition boards and LabView software. It was configured and interfaced with 48 NMDS detectors. After testing demonstrated that the system performed as desired, additional components, interfacing connectors and wires, were ordered to complete the 64-detector system. In addition, the NMDS was moved to a new detector laboratory at UNLV.

Figure 31. Data acquisition board for the NMDS.

The NMDS detectors were set up in a configuration that had been previously tested (see Figure 32), and background counts as well as counts with a low-strength source were taken. Although results compared favorably with previous NMDS counting data, discrepancies were noted between the two systems. The discrepancies will be investigated in the future. The group is preparing to re-configure the system in the B-cube geometry to calibrate it with a neutron-emitting standard and to measure cosmic neutron multiplicity under UNLV TRP Task 30.

Figure 32. NMDS configured in a cubic geometry for background and source counting. The Russian-built power supply and data acquisition systems are in the center back, and the new digital data acquisition board is in the right foreground (the computer is to the right of the picture).

Use of Positron Annihilation Spectroscopy for Stress-Strain Measurements (Task 14).

Cylindrical specimens of Alloys EP-823, HT-9 and 422, tested at different levels of tensile loading, have been analyzed by pair-production, activation and neutron diffraction techniques for characterization of residual stress resulting from plastic deformation due to applied loads between the yield strength and the ultimate tensile strength. The residual stresses in all three martensitic alloys in terms of the PAS line-shape parameters (S, W and T) exhibited consistent patterns.

The residual stress in terms of the S-parameter was gradually enhanced with increasing levels of plastic deformation at higher applied stresses. Conversely, the magnitude of the W and T-parameter was gradually reduced with increasing applied stress indicating higher residual stress in the tested specimens. The variations of S, W and T-parameters with applied stress, as determined by the pair-production method, are illustrated in Figures 33 and 34 for Alloys EP-823 and HT-9, respectively. Similar relationships of S, W and T-parameter to the applied stress were observed by the activation technique, as shown in Figures 35 through 37 for all three candidate target materials. Measurements on the tensile specimens of Alloy EP-823 by the ND technique exhibited higher residual stresses at increased level of applied stresses, as illustrated in Figure 38. Thus, the overall data revealed that, irrespective of the testing technique applied, the residual stress was enhanced at higher applied tensile loads.

The dislocation density (ρ) determined from the TEM micrographs of cold-worked plate materials was gradually enhanced by approximately an order of magnitude due to the reduction in thickness from 0 to 7-11, respectively, as shown in Figure 39.

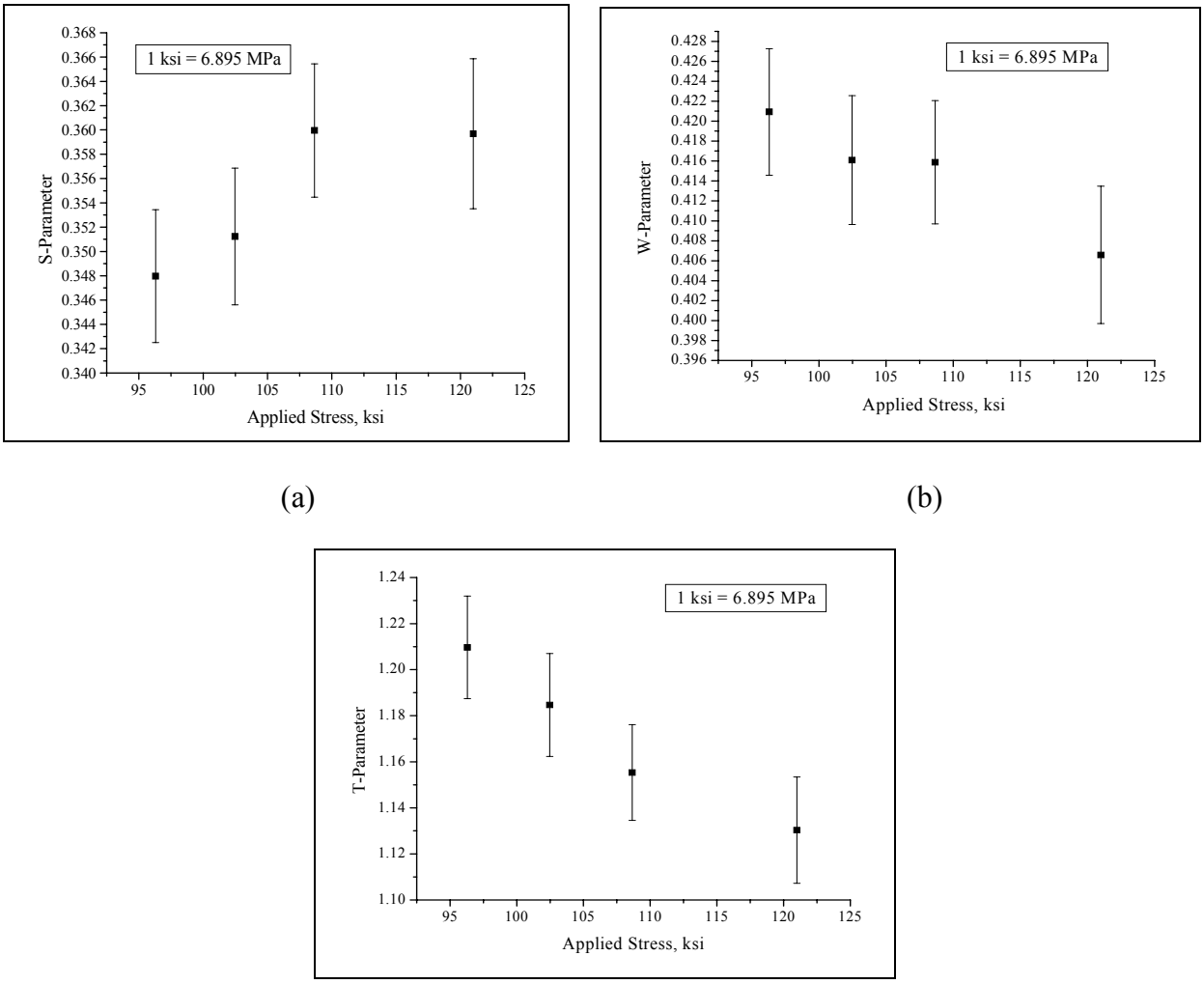

Figure 33. S, W, and T-Parameter vs. Applied Stress for Alloy EP-823 (Pair-Production).

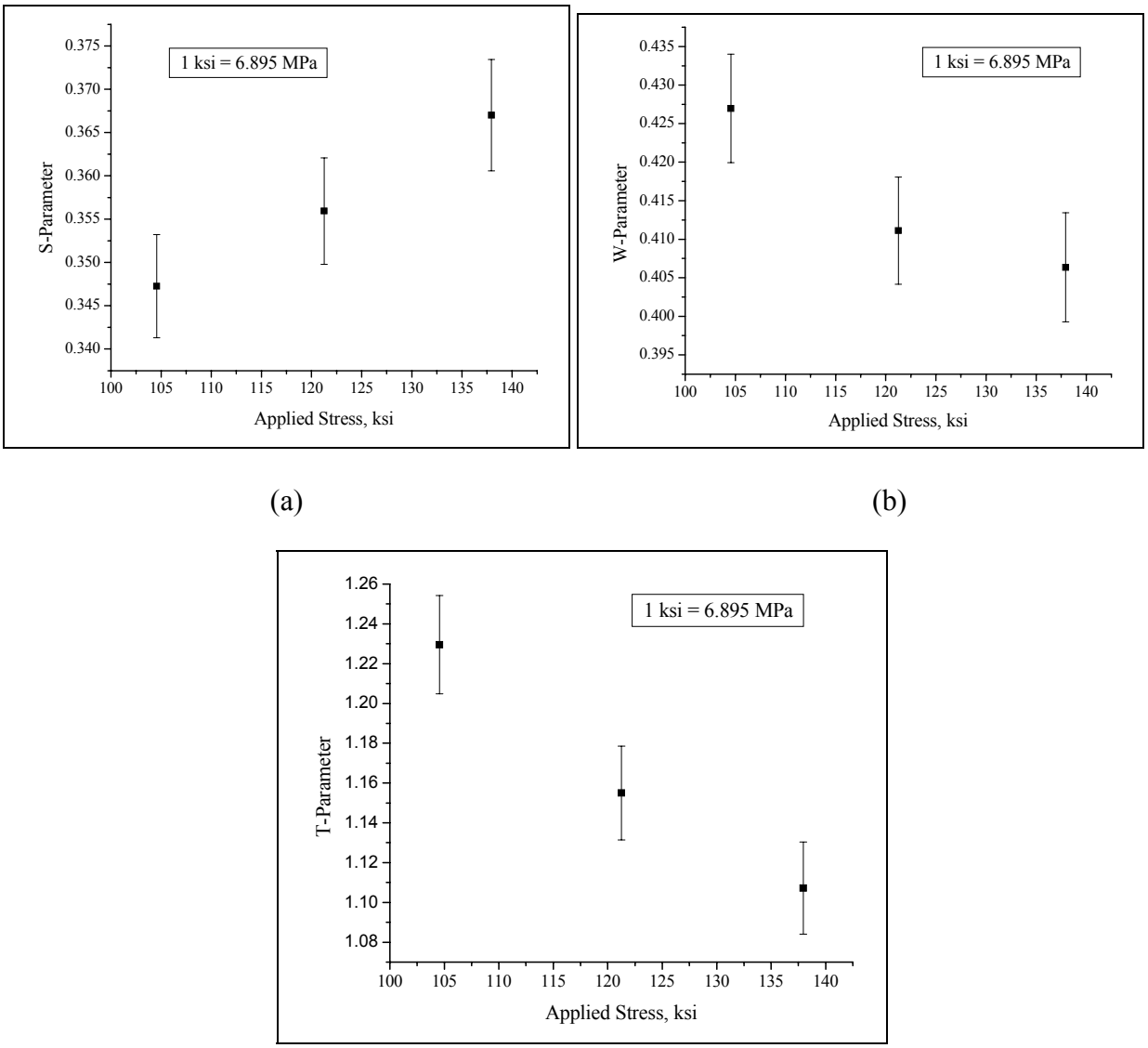

Figure 34. S, W, and T-Parameter vs. Applied Stress for Alloy HT-9 (Pair-Production).

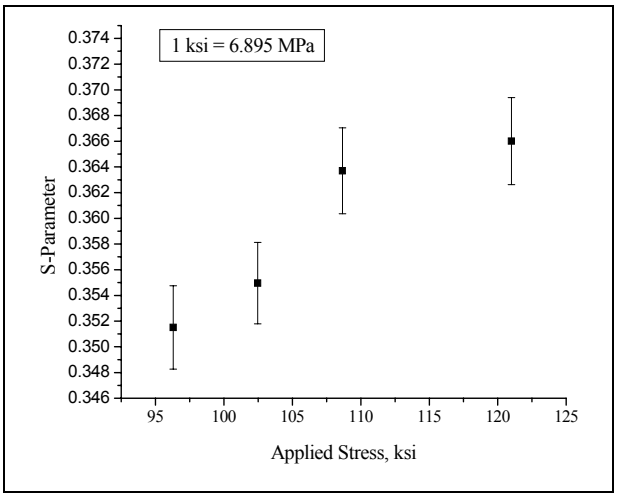

(a)

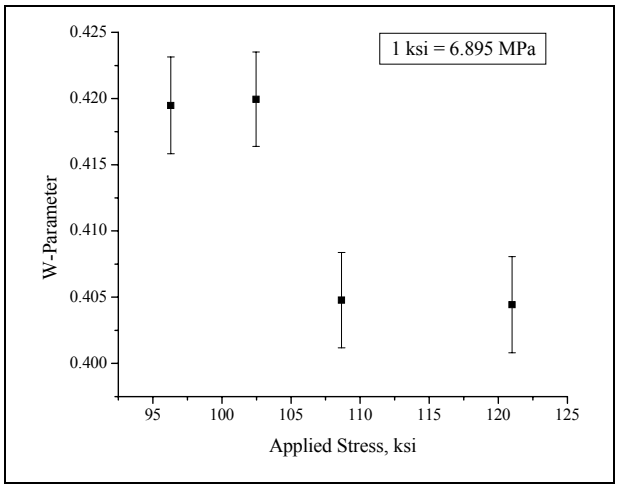

(b)

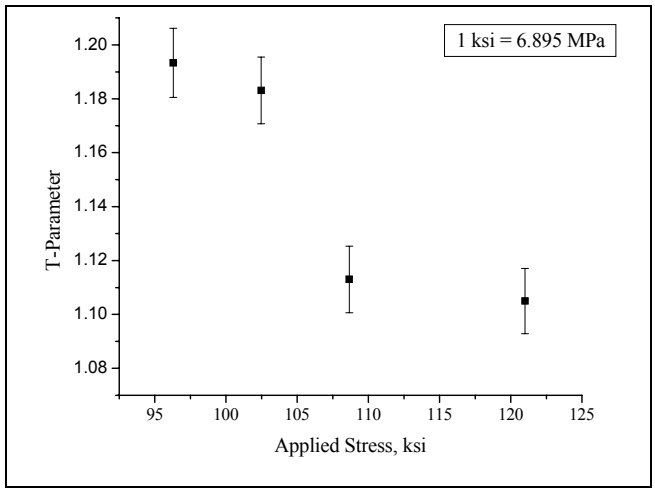

(c)

Figure 35. S, W, and T -Parameter vs. Applied Stress for Alloy EP-823 (Activation).

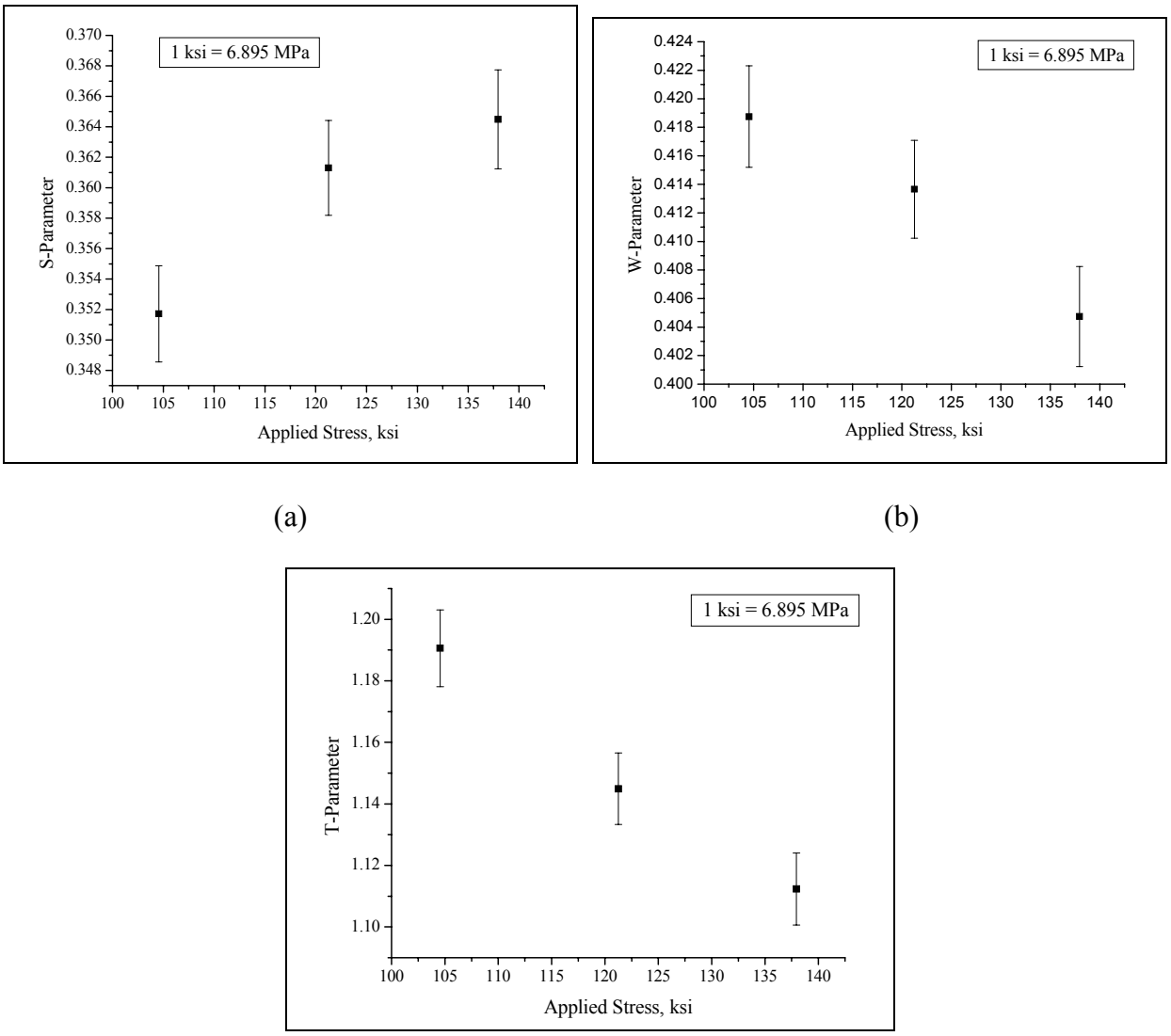

Figure 36. S, W, and T-Parameter vs. Applied Stress for Alloy HT-9 (Activation).

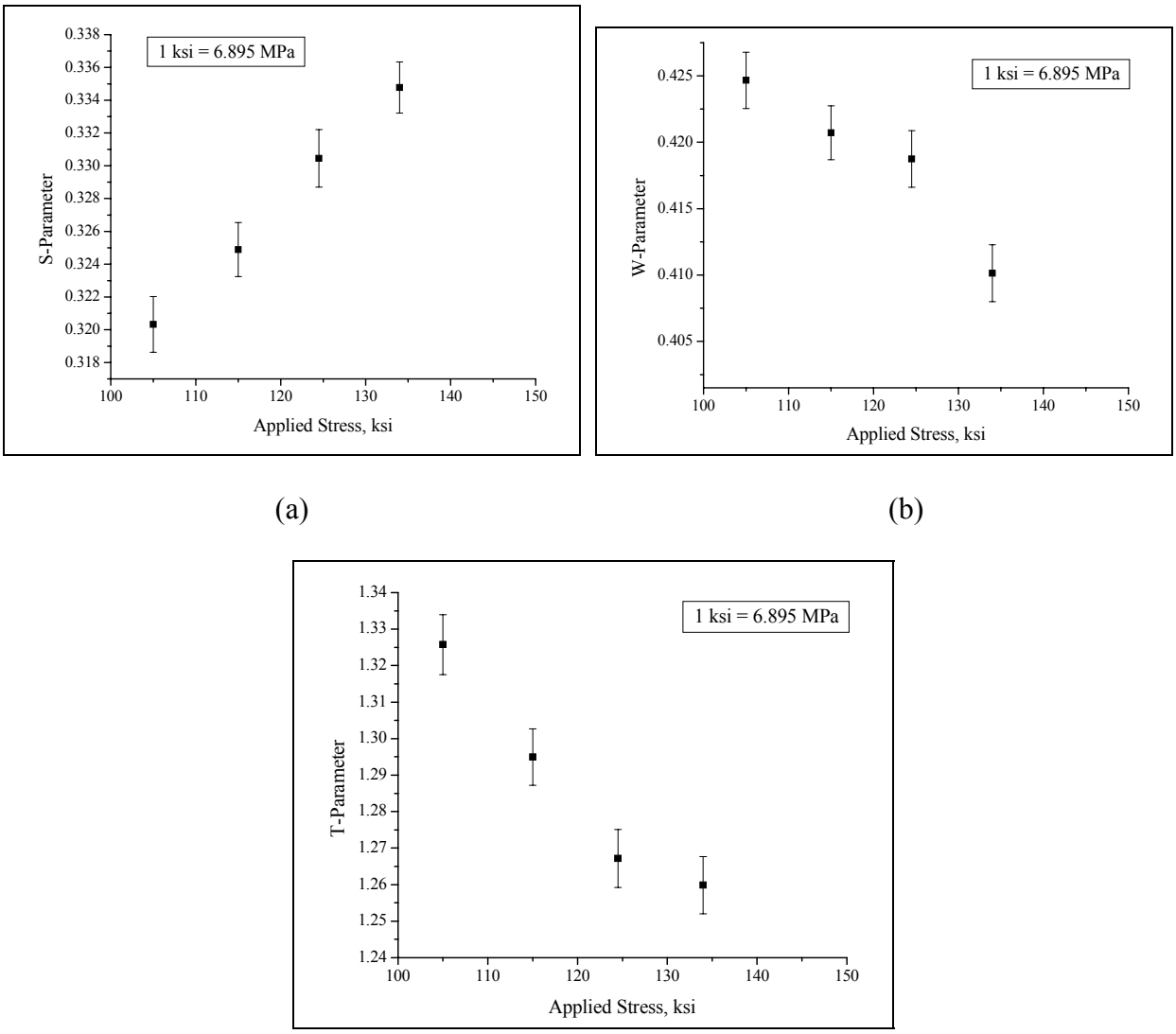

Figure 37. S, W, and T-Parameter vs. Applied Stress for Alloy 422 (Activation).

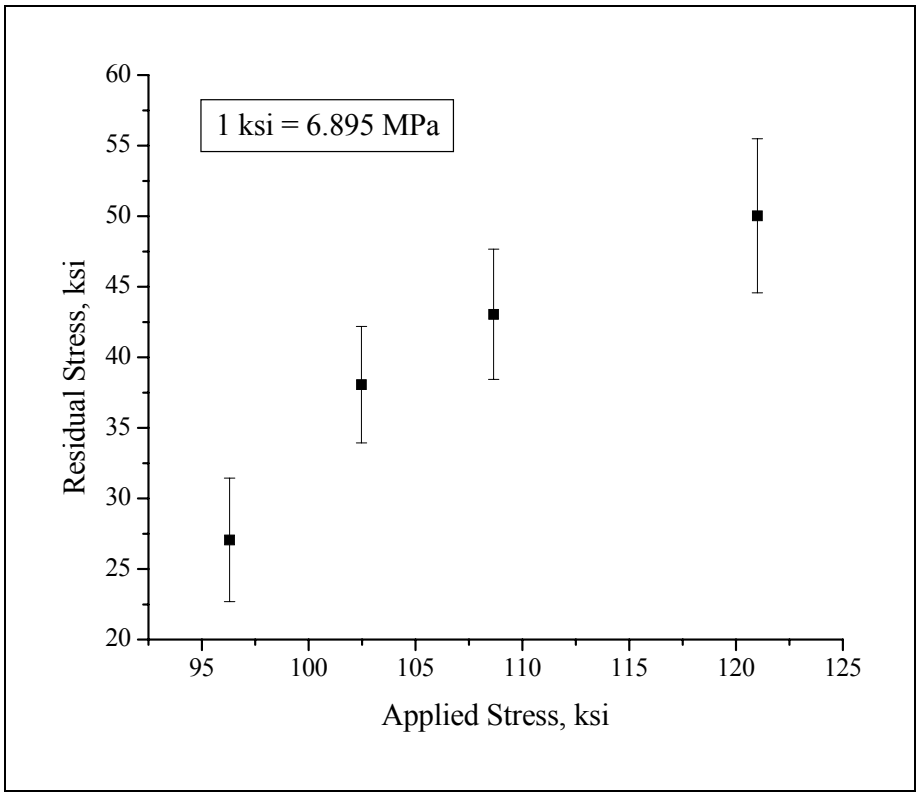

Figure 38. Residual Stress vs. Applied Stress (ND).

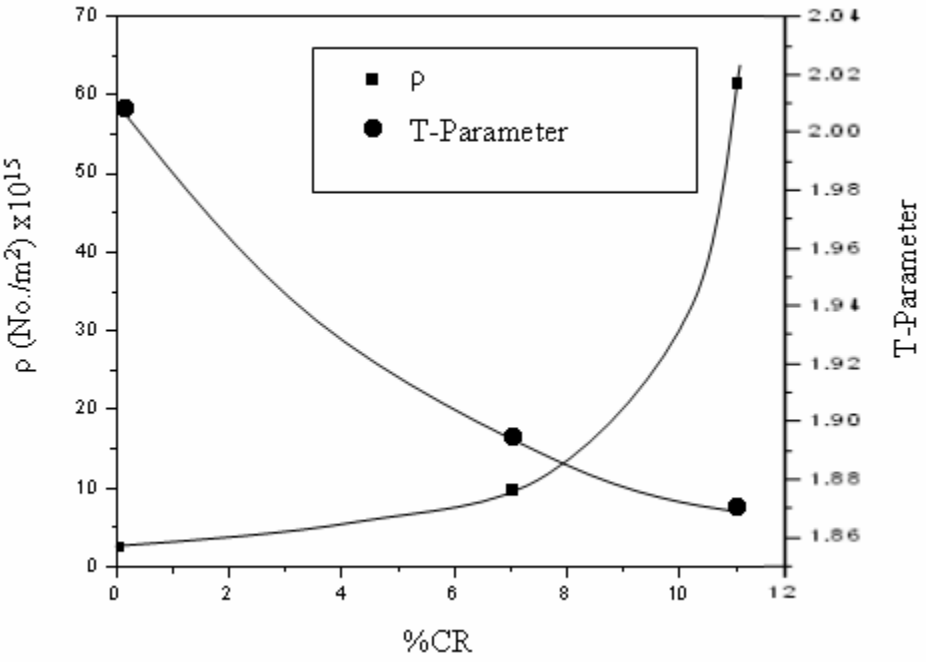

Figure 39. Variation of ρ and T- Parameter with Percent Cold-Reduction.

Corrosion Mechanisms and Kinetics of Steels in Lead-Bismuth Eutectic (Task 18).

In previous work, the LBE-induced corrosion of two samples of 316/316L standard nuclear grade steel having similar compositions but different surface treatments were compared. Corrosion rates at 550 C varied by an order of magnitude depending on surface preparation. The group published work that compared a cold-rolled 316 and an annealed 316 sample, exposed at IPPE in Obninsk, Russia. The cold-rolled sample, which suffered much less corrosion, displayed a thin protective oxide high in chromium. The annealed sample displayed a thicker duplex oxide composed of a Fe_2O_3 layer above a Fe, Cr oxide. This result was surprising in view of the conventional wisdom that thick oxide layers are more protective than thin oxide layers. However, these results are consistent with the results of other workers in the field.

The corrosion of D-9 (a 316 variant) by lead-bismuth eutectic (LBE) at elevated temperature was investigated using SEM, XPS with sputter depth profiling, and TEM after 1000 h of exposure to LBE at a temperature of 550 C. The process by which thin oxide evolves into extensive duplex oxide was probed. Under the experimental conditions, iron was observed to migrate outward through the nonprotective ion-chromium oxide layer, while chromium does not migrate. Intrusions of lead into and below the oxide layer were observed. The D-9 samples examined were closer to the annealed samples in their overall corrosion rate than to the cold-rolled samples. Parts of the oxide layer looked like the cold-rolled samples, while parts looked like the annealed samples. With continued exposure, duplex oxide grew everywhere.

Corrosion of D9 appears to occur in patches which grow until they cover the entire alloy surface (Figure 40). These patches in cross section (Figure 41) show several relevant features. First, the outer oxide is composed primarily of iron oxide, with small contributions from other components whereas the inner oxide is a mixed iron and chromium oxide. The interface between the oxides follows the original metal surface – indicating that the chromium that characterizes the inner oxide is not mobile under these conditions. The appearance of an inner oxide underneath the thin oxide indicates that the oxygen is fairly mobile in the inner oxide (spreading faster than the iron oxide in the outer layer). The fact that the oxide layers are forming patches indicates that the duplex oxide layer is started at a localized point defect, and that the failure of the thin oxide spreads from there.

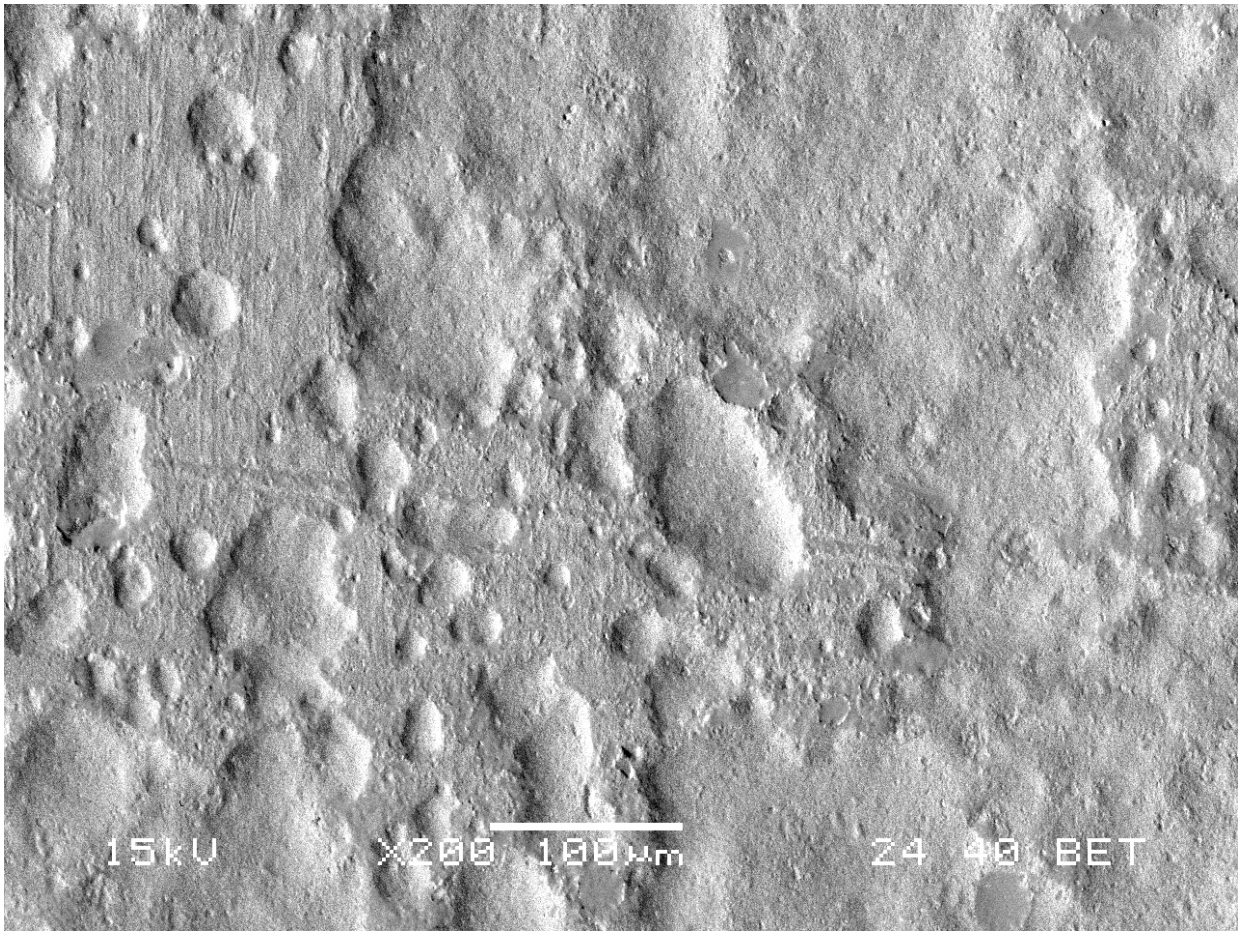

Figure 40. Patchy oxide on the surface of D9 exposed to LBE.

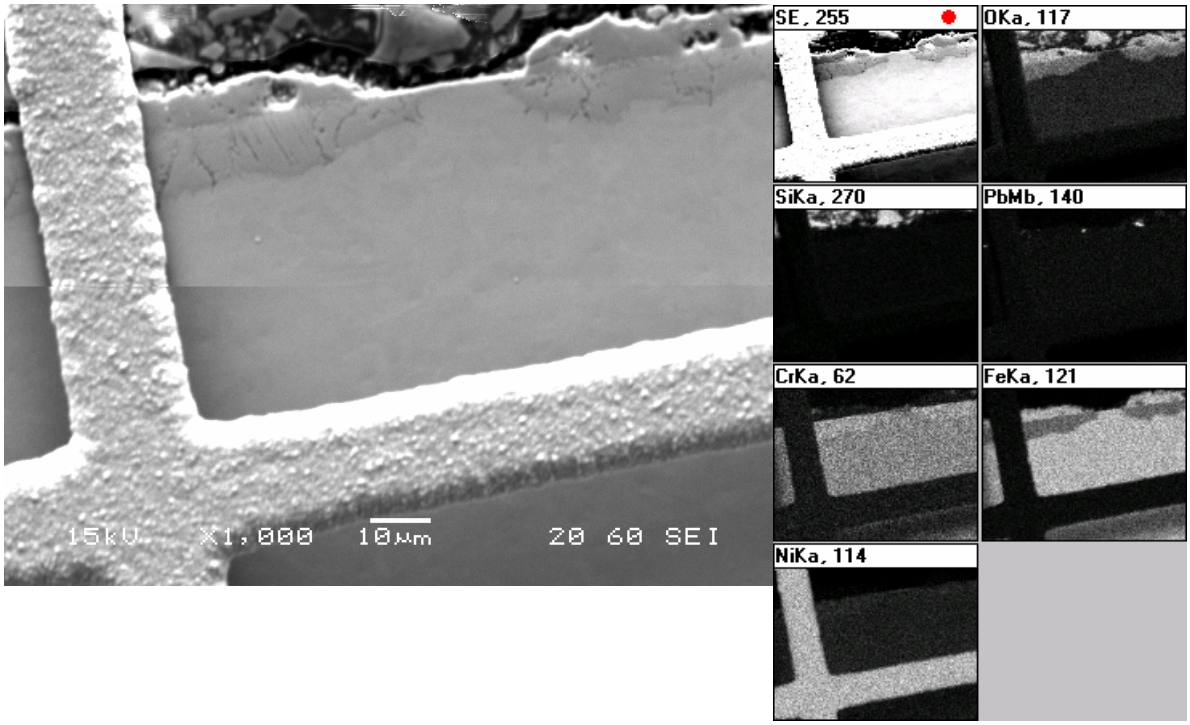

D9 1000 hr

Figure 41. Transverse section of D9 corrosion. Note that the boundary between the outer oxide and the inner oxide follows the original metal surface. Further, the inner oxide grows underneath the thin oxide before being covered by the outer oxide.

The thin oxide is more difficult to characterize. XPS and sputter depth profile investigations were performed that show that the thin oxide is very similar to the oxide found on the cold rolled 316 samples studied previously. TEM investigations (Figure 42) of the thin oxide in cold rolled 316L show layer spacings similar to the unit cell size for $FeCr_2O_4$, Chromite. STEM EDX measurements of the thin oxide in cold rolled 316L indicate the presence of iron and chromium in the thin oxide as well. A depletion of chromium was observed underneath the thin oxide by all of the techniques, and the results are being compared.

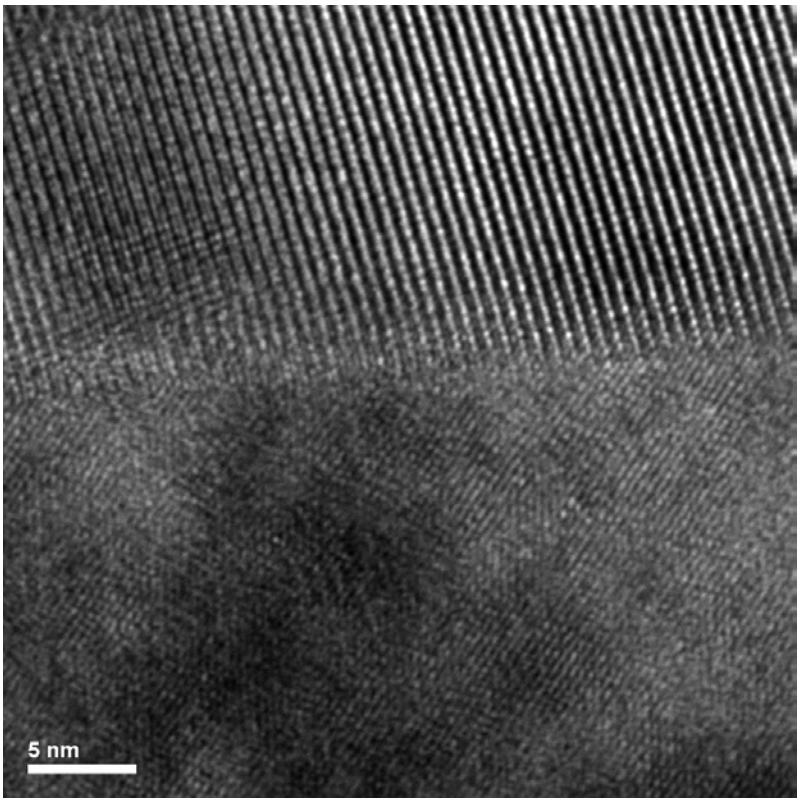

Figure 42. TEM image of the oxide-metal interface in cold rolled 316L. The oxide layer is on top of the alloy substrate. The layer spacing in the thin oxide is consistent with the ~8 angstrom unit cell of $FeCr_2O_4$, chromite.

Etching the sample to reveal grain boundaries and crystal defects show more detail of the oxide growth dynamics (Figure 43). The inner oxide grows preferentially along grain boundaries in the alloy, and there is evidence of grain defects (either boundaries or other defects) in the inner oxide that form pathways for oxygen transport. The outer oxide seems rather amorphous in comparison.

The finding that the onset of duplex oxide formation occurs at point failures, and the observation of depletion of chromium underneath the thin oxide leads to the speculation that enhancement of the availability of chromium underneath the thin oxide may be the mechanism for the stability of 316 cold rolled verses 316 annealed as well as suggest that such strategies for other chromium containing alloys may be useful.

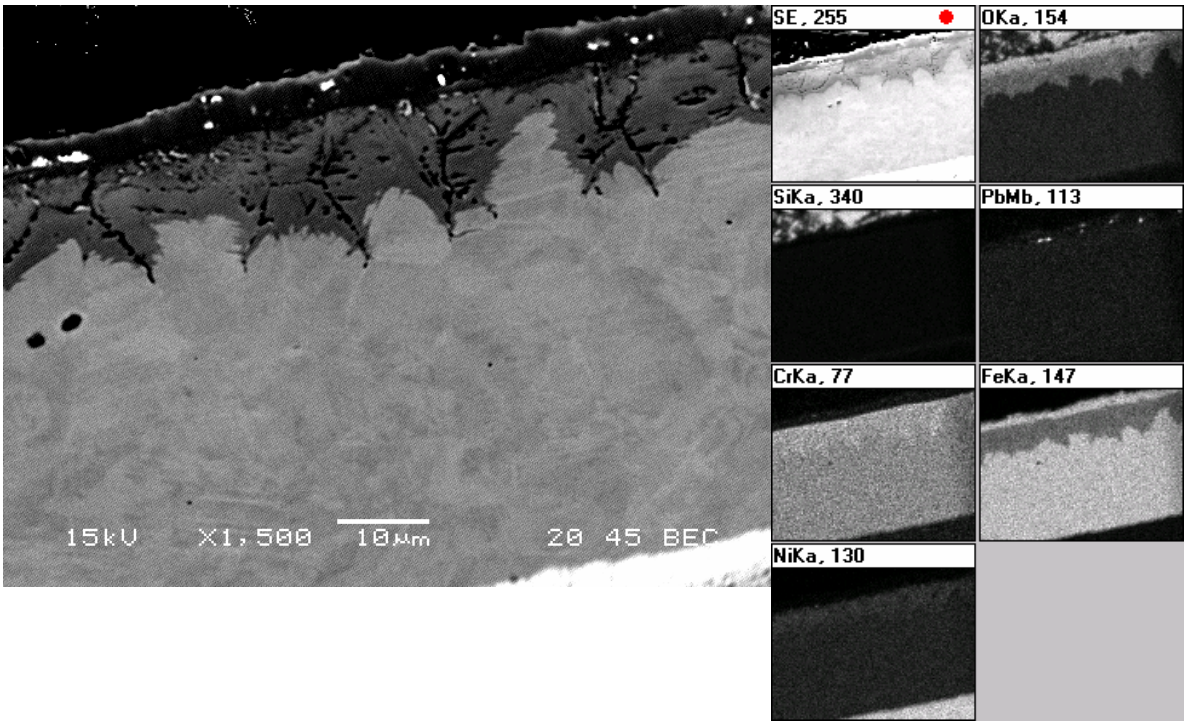

Figure 43. D9 etched to show grain boundaries. Note the enhanced growth of the inner oxide along alloy grain boundaries and the channels for oxygen migration between and inside oxide grains.

Impact of Silicon on Corrosion Resistance of Stainless Steels in LBE Systems (Task 20).

The purpose of this collaborative research project involving the University of Nevada Las Vegas (UNLV), Los Alamos National Laboratory (LANL) and Idaho State University (ISU) is to evaluate the effect of silicon (Si) content on the corrosion behavior and radiation-induced embrittlement of martensitic stainless steels having chemical compositions similar to that of the modified 9Cr-1Mo steel. Recent studies at LANL involving Alloy EP-823 of different Si content have demonstrated that increased Si content in this alloy may enhance the corrosion resistance in molten lead-bismuth-eutectic (LBE). Since very little data exists in the open literature on the beneficial effect of Si content on the corrosion properties, it seemed appropriate to initiate a research project to address this technical issue.

Tensile properties of T91 grade steel with 1 and 2 wt% Si content were evaluated at temperatures ranging between ambient and 550^{o}C. The engineering stress versus strain (s-e) diagrams for both alloys are shown in Figures 44 and 45 as a function of the testing temperature. As expected,

the magnitude of the yield strength (YS) and ultimate tensile strength (UTS) was gradually reduced with increasing temperature.

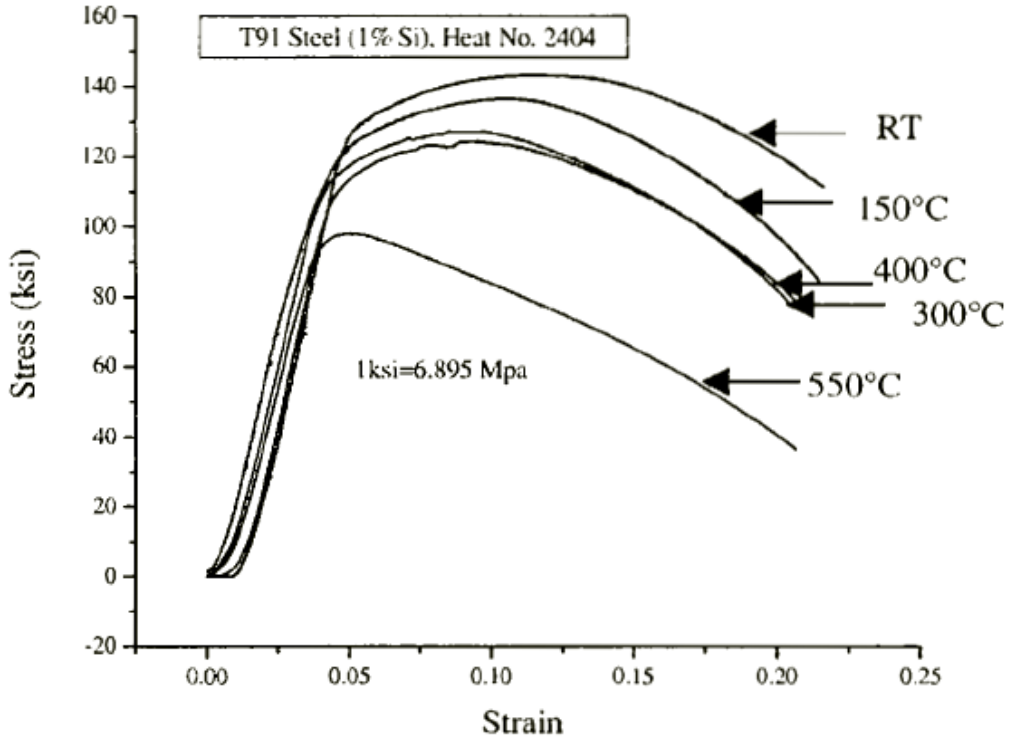

Figure 44. Stress-strain diagrams at different temperatures for T91 steel with 1 wt. % Si.

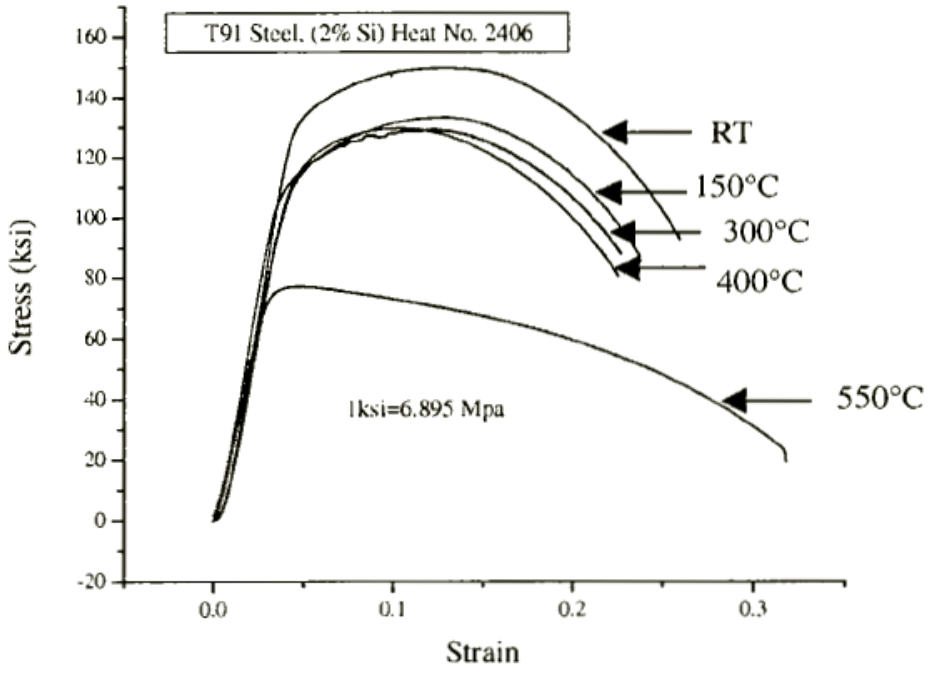

Figure 45. Stress-strain diagrams at different temperatures for T91 steel with 2 wt. % Si.

The extent of failure strain (e_f) was not significantly affected by the variation in the testing temperature for steel containing 1 wt% Si. However, the failure strain for the higher Si-containing alloy was gradually reduced up to 400°C, followed by a significant increase at 550°C, as shown in Figure 45. The gradually-reduced e_f in the later case may be attributed to the dynamic strain-ageing effect. The variation of YS, UTS, percent elongation (%El), and percent reduction in area (%RA) with temperature is illustrated in Figures 46 through 49.

The results of stress corrosion cracking (SCC) tests involving T91 grade steels containing 1 and 2 wt% Si at constant load indicate that neither alloy exhibited failure in an acidic solution irrespective of the testing temperature.

The s-e diagrams obtained in SCC testing under a slow-strain-rate (SSR) condition in an identical environment are shown in Figures 50 and 51 for both alloys at different temperatures. Both figures indicate enhanced cracking susceptibility at elevated temperatures. The magnitudes of %El, %RA, time-to-failure (TTF), and the true failure stress (σ_f) obtained from the SSR testing were gradually reduced with increasing temperature.

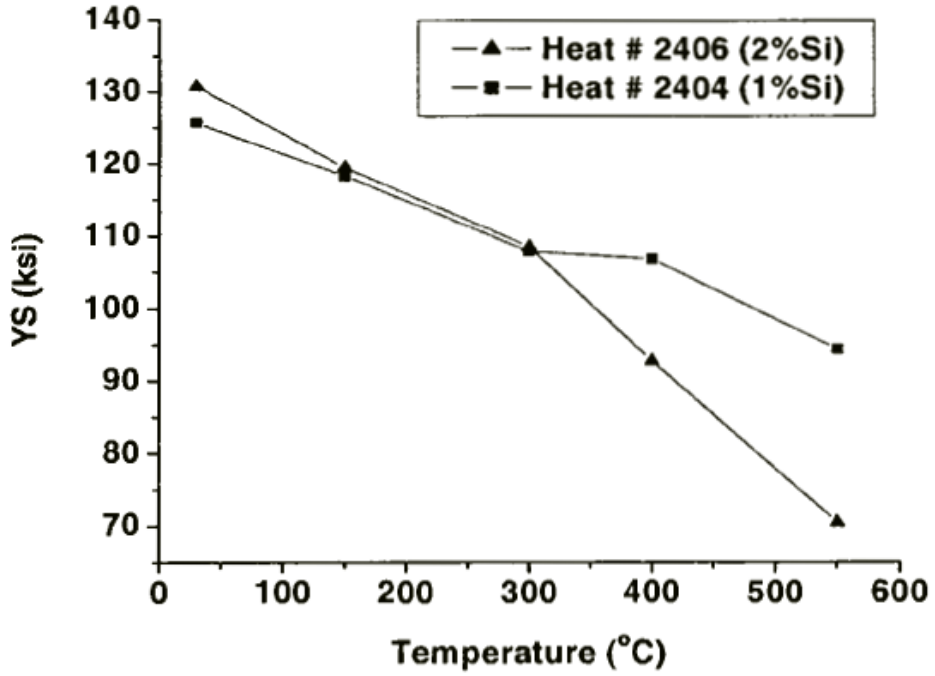

Figure 46. Yield strength versus temperature.

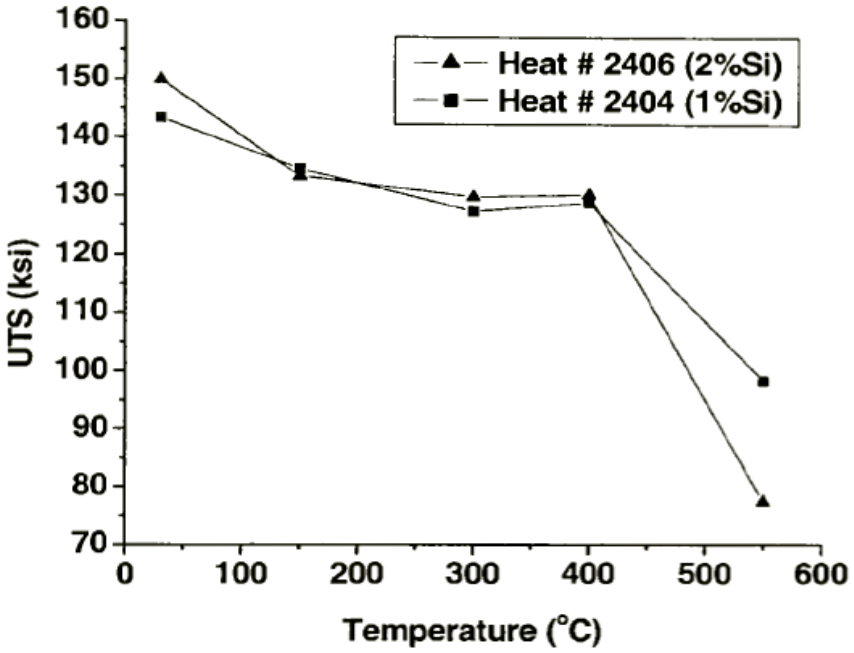

Figure 47. Ultimate tensile strength versus temperature.

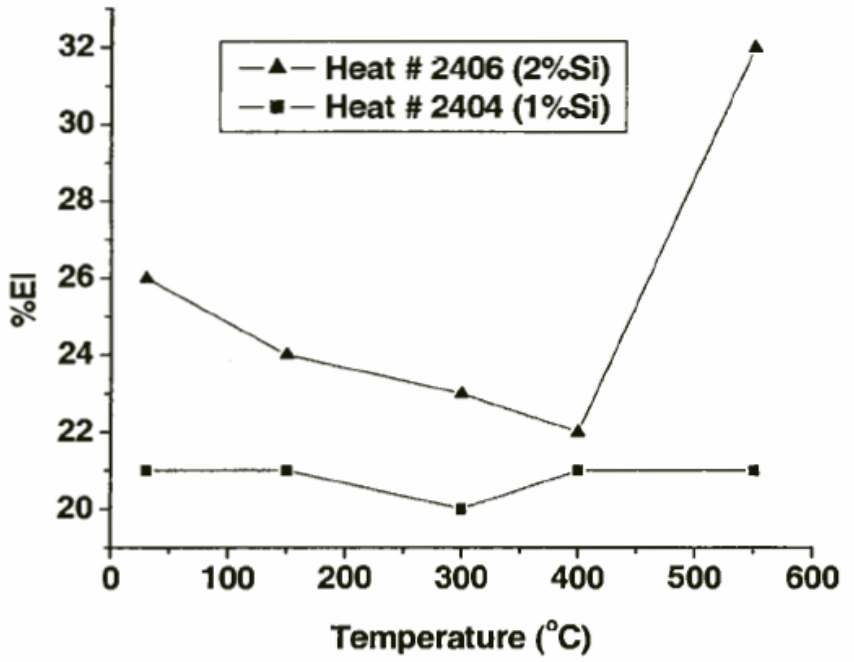

Figure 48. Percent elongation versus temperature.

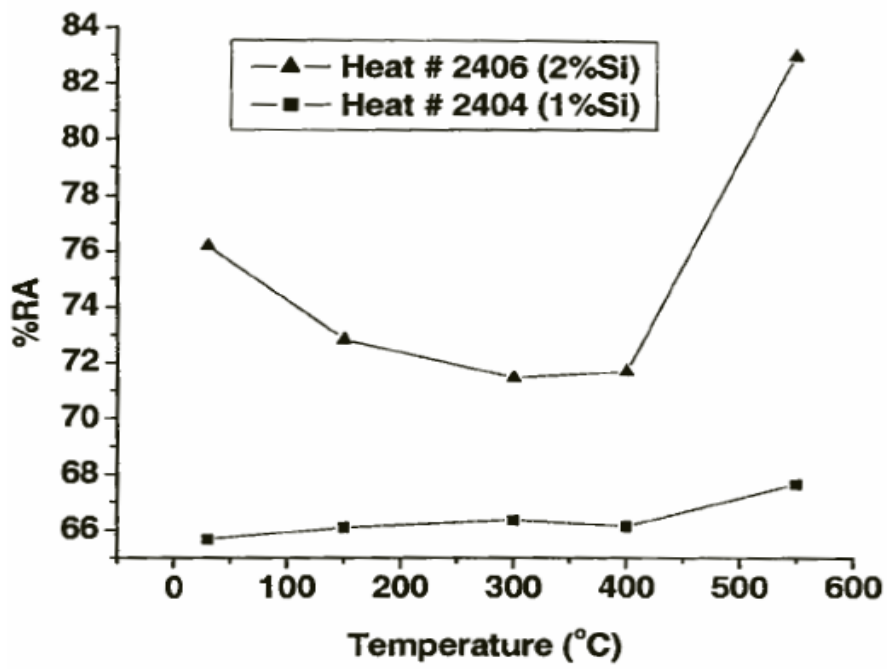

Figure 49. Percent reduction in area versus temperature.

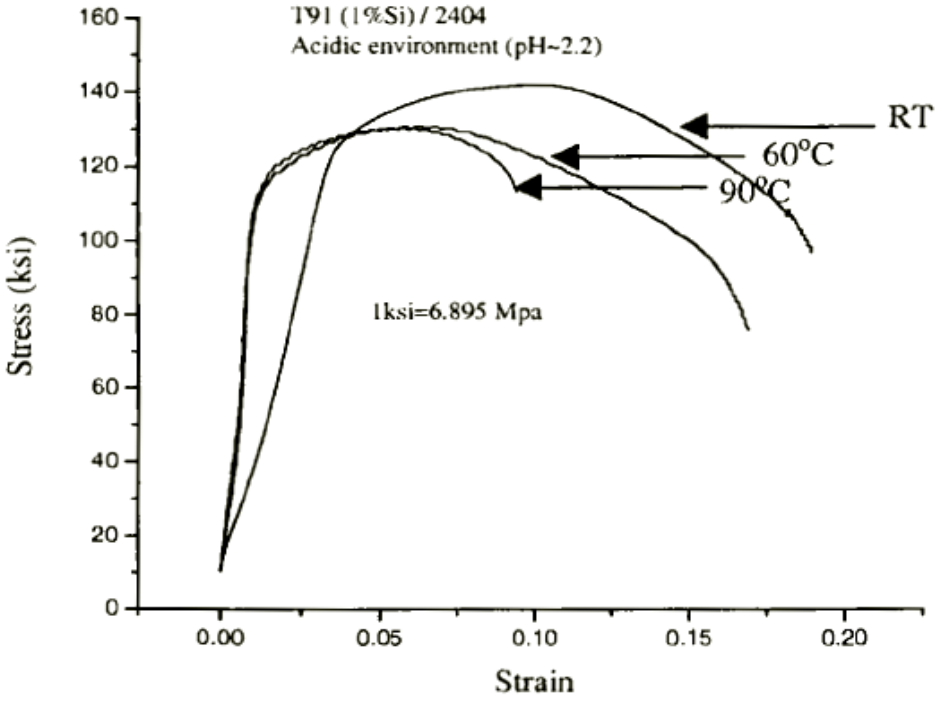

Figure 50. Stress-strain diagrams for different temperatures.

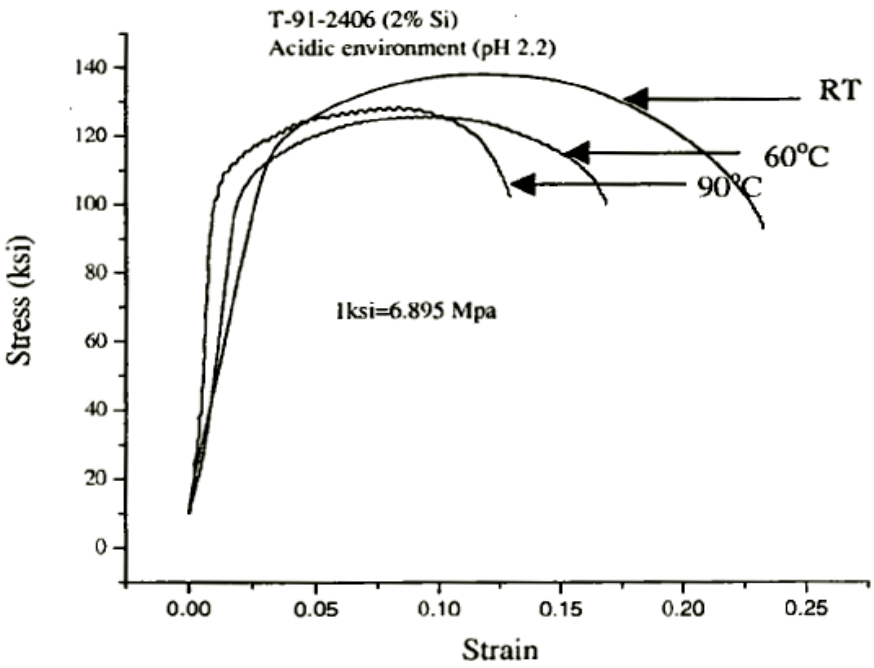

Figure 51. Stress-strain diagrams at different temperatures.

The results of localized corrosion studies by cyclic potentiodynamic polarization technique exhibited an active-passive behavior with a positive hysteresis loop, as shown in Figure 52. In general, the corrosion potential (E_{corr}) became more active (negative) with increasing temperature.

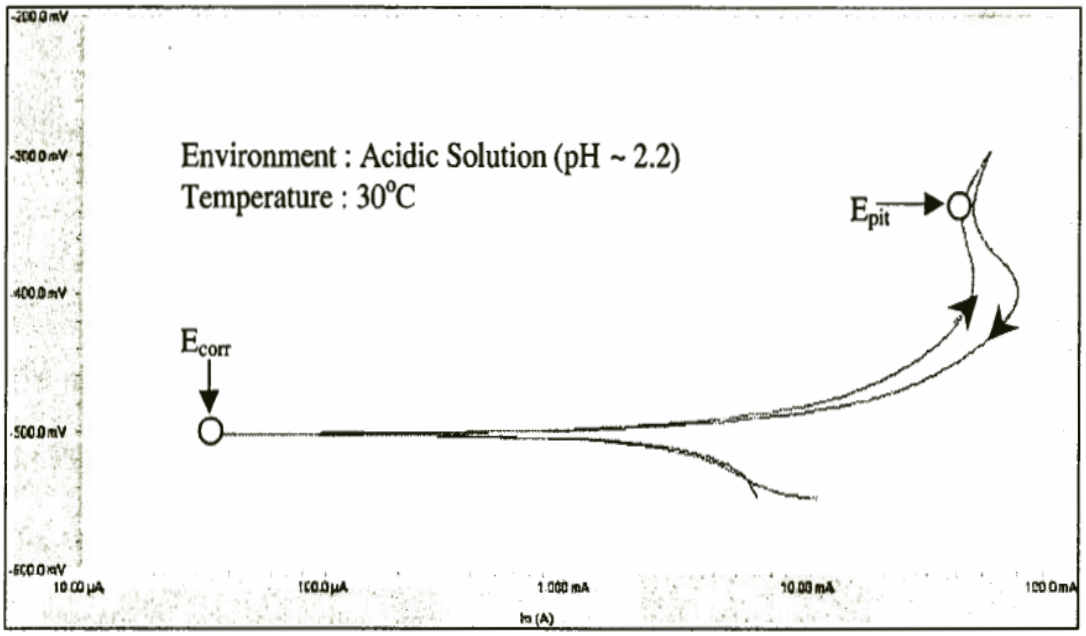

Figure 52. CPP Diagram of T91 Grade Steel Containing 1 wt% Si.

Fractographic evaluations of the cylindrical specimens, used in SSR testing, by scanning electron microscopy revealed brittle (intergranular and transgranular) failures in T91 grade steel containing 1 wt% Si, as shown in Figures 53. However, ductile failures were observed in the higher Si-containing steel at 30 and 60^{o}C, as illustrated in Figure 54. At 90^{o}C, a combination of ductile and brittle failures was observed.

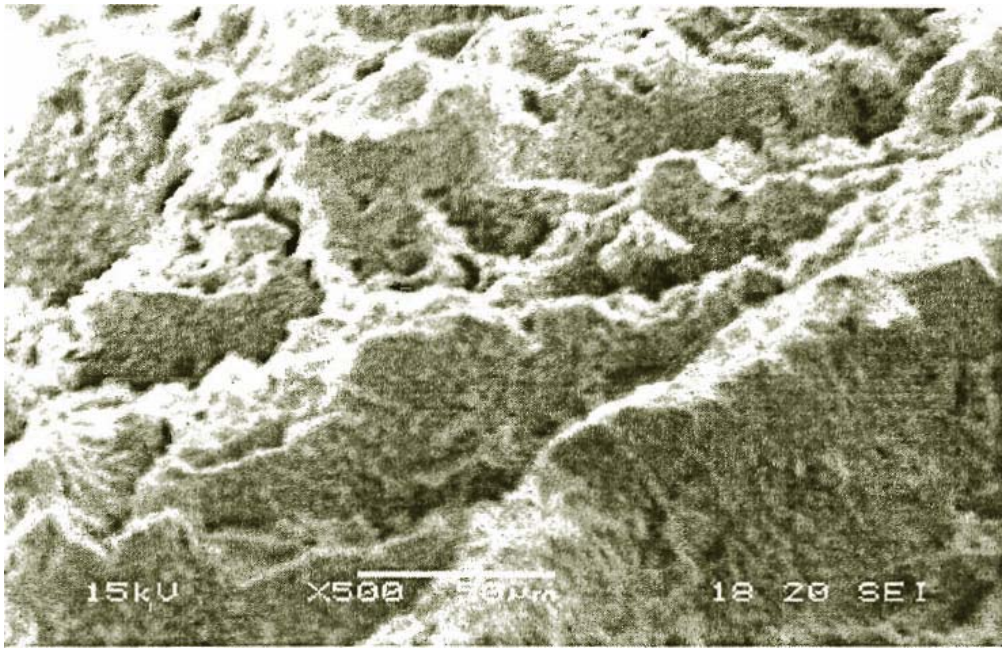

Figure 53. SEM Micrograph of T91 Grade Steel (1 wt% Si) at RT, 500X.

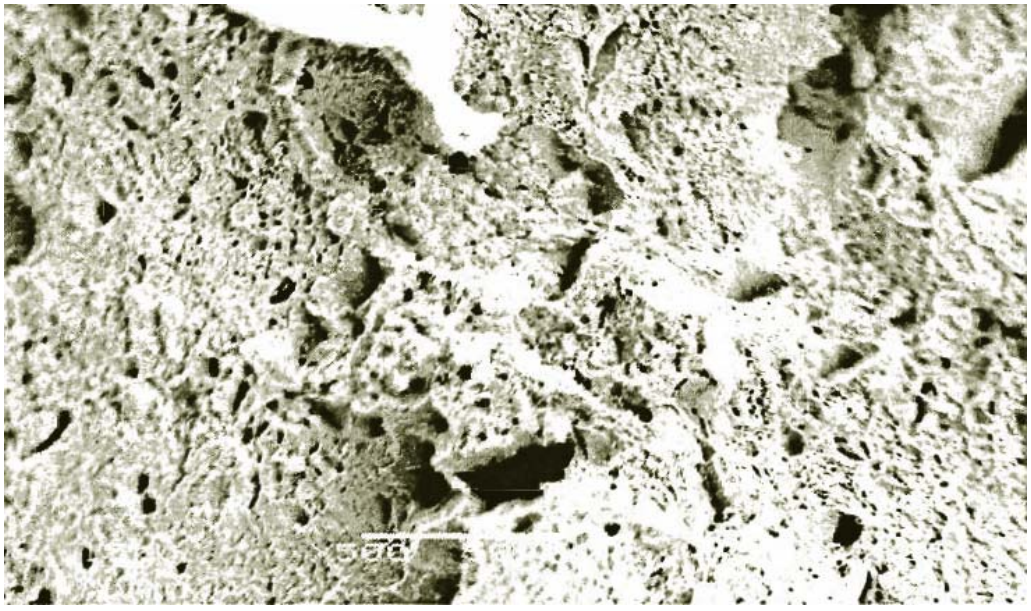

Figure 54. SEM Micrograph of T91 Grade Steel (2 wt% Si) at RT, 500X.

Oxide Film Growth Modeling in LBE Systems (Task 21).

Lattice Boltzmann simulation on the enhancement of oxygen transport by forced convection

The enhancement of oxygen transfer by forced convection has been investigated in detail. Three kinds of different force convection models have been considered. The Lattice Boltzmann simulations of the forced convection driven oxygen transfer in the liquid lead and LBE are presented.

Since the oxygen diffusion time is much longer than the developing of velocity, the unsteady terms for the momentum transport can be neglected. The steady-state velocity distributions are demonstrated in Figure 55 for three different inlet-outlet locations at Re = 1143. Similar patterns are shown at higher Re. As seen in Figure 55, the location of inlet and outlet obviously changes the convection flow. For case A, the LBE flow is injected near the bottom wall and passes through the container at the outlet near the top wall. One counterclockwise rotating flow cell is generated in the left-top corner region. The velocity vector plots of case B show that there is a counterclockwise rotating flow cell in the left-top corner region while a clockwise rotating flow cell occurs at the right-bottom corner. For case C, the LBE fluid flows along the free surface and then passes through the container at the outlet near the bottom wall. One clockwise rotating flow cell forms at the right-bottom corner. Since oxygen concentration at the free surface is much larger than that inside the container, it is expected that these circulated flow cells can mix the oxygen quickly and then enhance the oxygen transport.

Once the oxygen controlled technique is applied to mitigate corrosion, one important task is to find a way to mix oxygen in a low concentration uniformly and quickly. In this section, emphasis is placed on the forced convection of the oxygen transport and the consumption of the oxygen on the wall is neglected. To render the oxygen concentration dimensionless, the oxygen concentration is normalized by the dissolving oxygen concentration at the liquid surface.

Figure 56 shows the oxygen concentration contours at different times (t = 40, 150, 350, and 1000 s) for different case at Re = 1143 and Sc = 5. The concentration contours at $t \geq 350$ s for each case are similar to their velocity distributions shown in Figure 55. This clearly shows that force convection is the dominant driving force for oxygen transfer. From all the figures, it can be found that a flow cell can evidently enhance the oxygen transport. At t = 40 s, it is noted that oxygen first spreads along the left side wall of the container from the free surface for case A due to the counterclockwise rotating flow cell. As time increases, oxygen continues to transfer from the upper part to the lower part and fills the entire region of the container gradually. Under case B, the oxygen transport in the right bottom corner is much faster since the clockwise rotation cell occurs. Similar phenomena can also be found in case C.

To test and calibrate oxygen sensors, the oxygen sensors will be placed at three columns inside the container ($x = 0.25L$, $0.5L$, and $0.75L$). The oxygen concentration at oxygen sensor locations at different times is illustrated in Figure 57 for different Sc numbers at Re = 1143 and Sc = 5 for different cases. As found in the figures, the oxygen concentration at different locations increases as time increases. For all the cases, the variation of oxygen concentration with time changes. Since the convection is the dominant force for oxygen transport, all of the phenomena can be

well explained by checking the flow pattern. From all of the curves, it is noticed that the variation or gradient of oxygen concentration in the location near the upper free surface is smaller compared to further away from the free surface since the mixture of hydrogen and water steam covers the upper free surface. Hence, it is better to locate the oxygen sensor a certain distance away from the free surface to get good measurement. For case A, since the counterclockwise rotation flow cell at the left-top corner is closer to the interface, the oxygen concentration transport here is much faster than that in the other region. A similar situation can also be found in case B. From the figures, it can be found that the oxygen transport at case C is more uniform compared to the other cases.

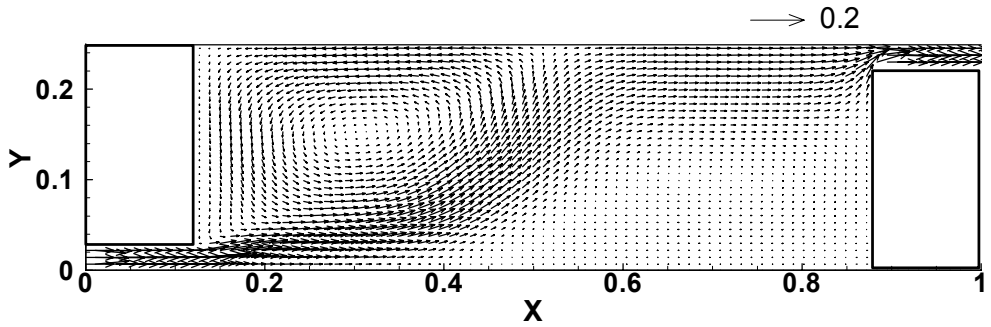

(a) Case A

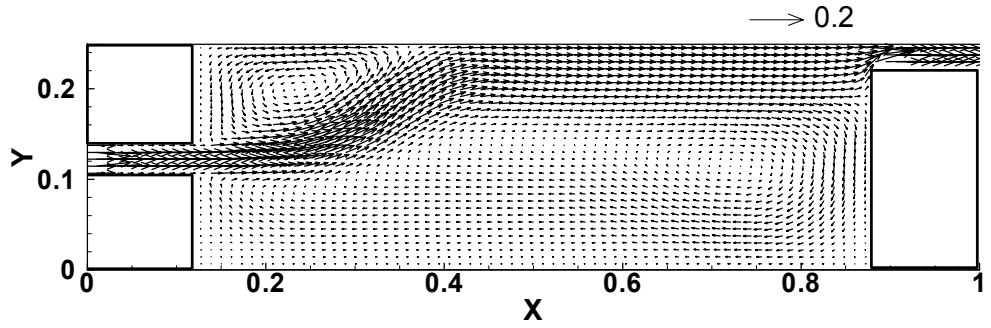

(b) Case B

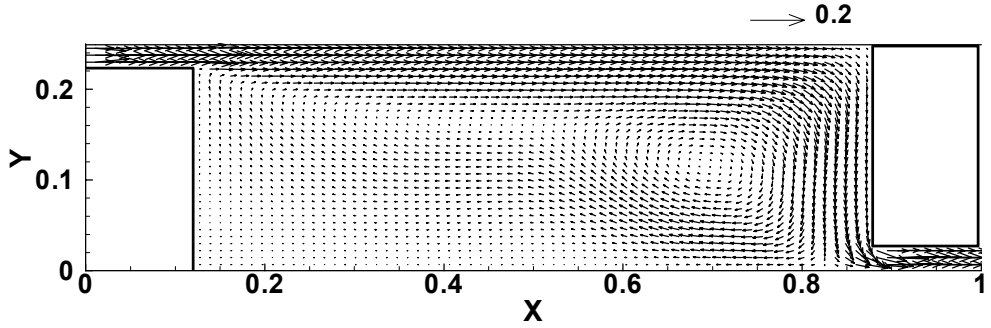

(c) Case C

Figure 55. Flow pattern under different forced convection mode (Re = 1143).

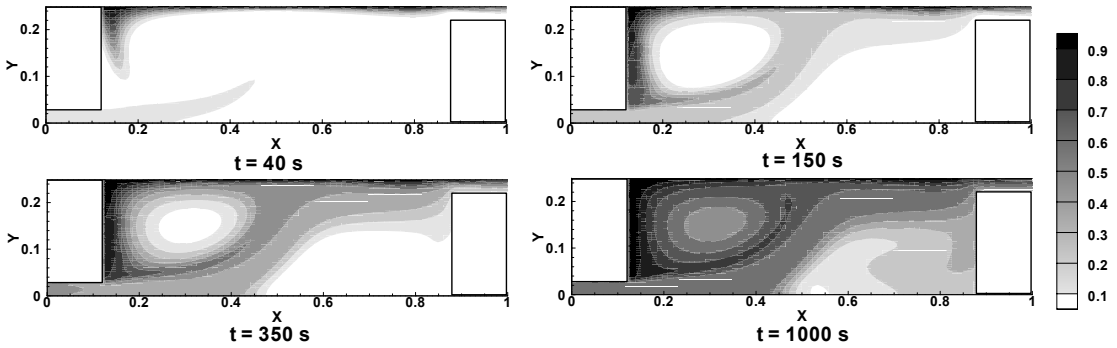

(a) Case A

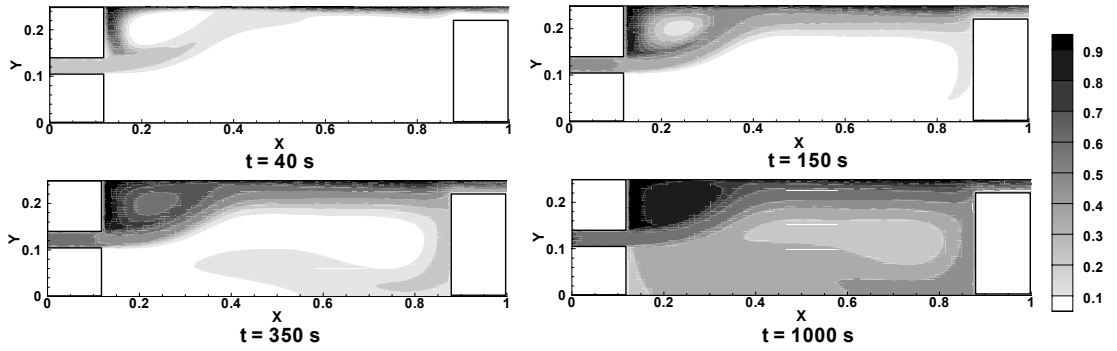

(b) Case B

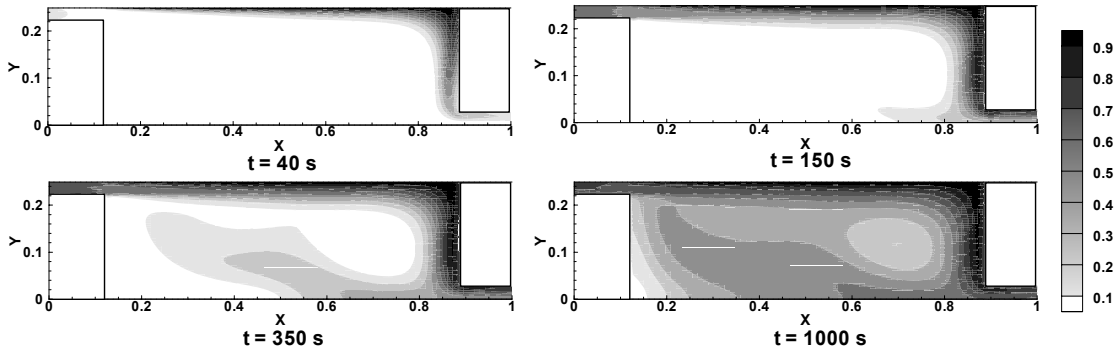

(c) Case C

Figure 56. Oxygen concentration contours at different times (t = 40, 150, 350, and 1000 s) for different convection mode. Re = 1143 and Sc = 5 for all cases.

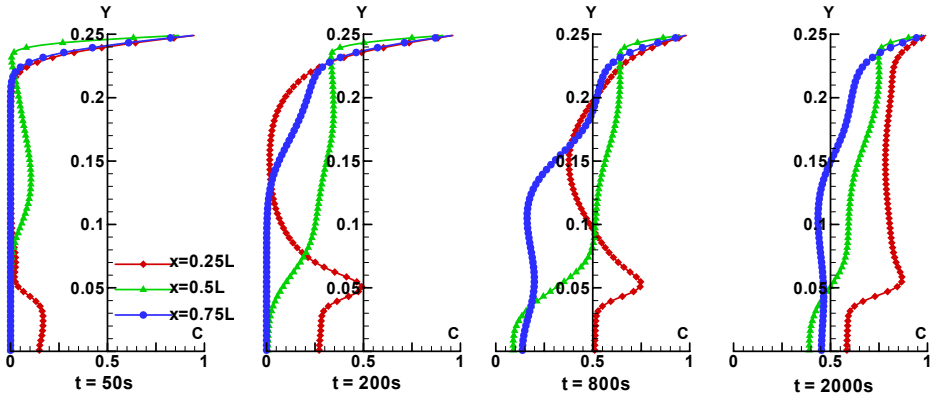

(a) case A

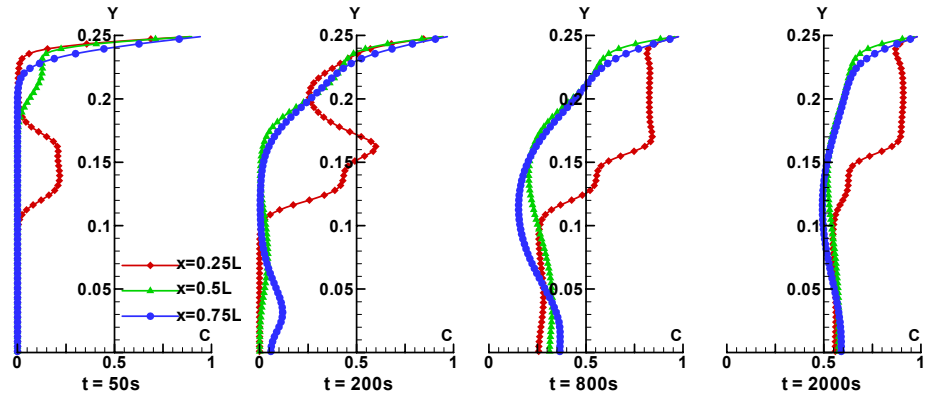

(b) case B

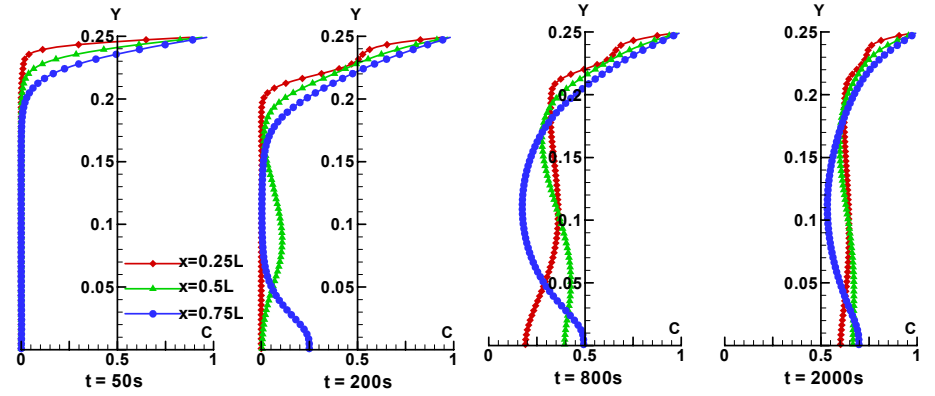

(c) case C

Figure 57. Oxygen concentration at oxygen sensor locations at different time. Re = 1143 and Sc = 5 for all cases.

To check the oxygen transfer speed, the bulk concentration was examined under different heating conditions, as shown in Figure 58. For all cases, the bulk oxygen concentration increases with increasing time. At the initial period, the bulk oxygen concentration will increase sharply and the effect of convection on oxygen transfer is more intense. Of these three temperature boundary conditions, case C seems to be the fastest way to get equilibrium for oxygen transfer as compared to the other cases, although bulk oxygen concentration for case A in the initial stage is

faster. Figure 58 also indicates that natural convection can enhance oxygen transfer. It takes about ~ 10^4 s for the oxygen concentration to reach ~ 90% of the input concentration from the top for case C at Re = 1143 and Sc = 5 while the pure diffusion would take ~ 10^6 s.

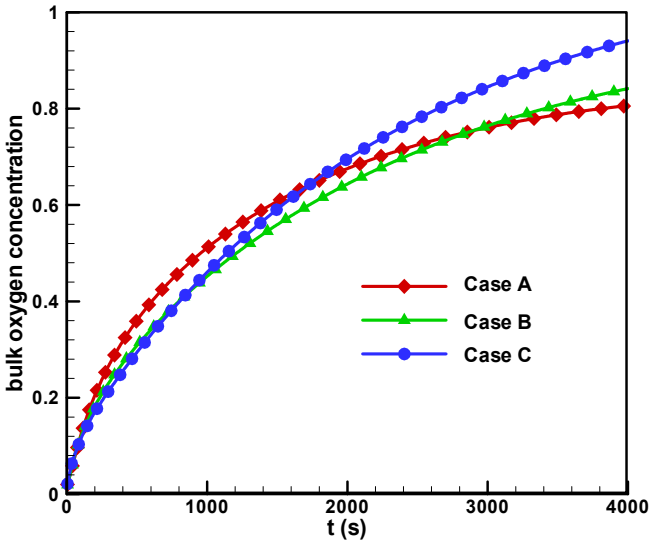

Figure 58. The bulk oxygen concentration in the liquid as a function of time for different boundary conditions. Re = 1143 and Sc = 5 for all cases.

Figure 59 shows the average Sherwood number at the interface of the cover gas and liquid metal as a function of time for different boundary conditions. The Sherwood number is defined by

$$Sh = \frac{KL}{D} = \frac{1}{1-\overline{C}_{bulk}} \frac{\partial \overline{C}}{\partial Y}\bigg|_{Free\ \ surface}$$

where $\overline{C}$ is the normalized oxygen concentration in the free surface and K is the mass transfer coefficient (m/s). For all cases, the average Sherwood numbers drop significantly with time during the first 200 s. After that, the average Sherwood number is almost constant for case A. However, for cases B and C, the average Sherwood number increases slightly as time increases and keeps constant after approximate 2000 s. From the figure, it can also be found that the Sherwood number in case C is larger than that in the other case after the initial stage. Considering that the larger Sherwood number corresponds to stronger mass transfer at the interface, more oxygen is transported into the liquid in case C compared to the other cases.

Theoretical analysis on oxidation accompanied by scale removal: initial and asymptotical kinetics.

General kinetics of oxidation associated with scale removal such as scale dissociation, volatilization, erosion, or mass transfer corrosion are analyzed employing the dimensionless Tedmon's equation. Expressions suitable for analyzing and fitting the oxide thickness/weight changes at early stages and long-term operations are presented. The scale of the time, the oxide thickness and the mass gain are specified. In addition, a perturbation solution showing the effects of the parabolic oxidation and the linear scale removal, and the combined effects of both

terms are obtained. The limitation of the perturbation solution is determined. Figure 60 shows the variation of non-dimensional thickness for different solutions.

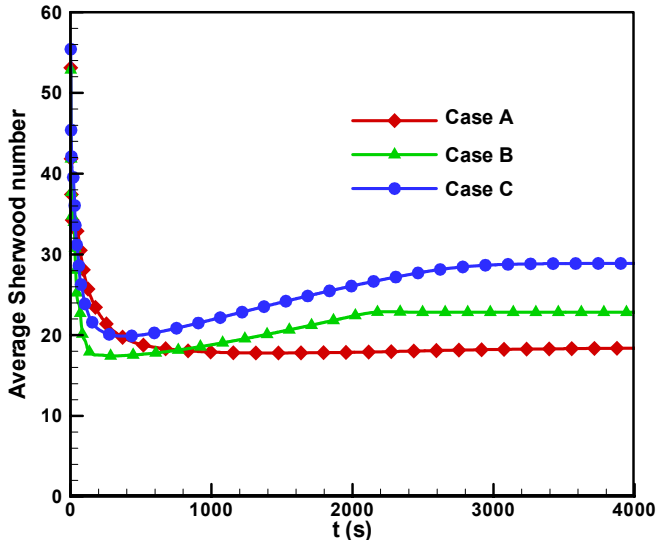

Figure 59. The average Sherwood number at the interface of cover gas and liquid metal as a function of time for different boundary conditions. Re = 1143 and Sc = 5 for all cases.

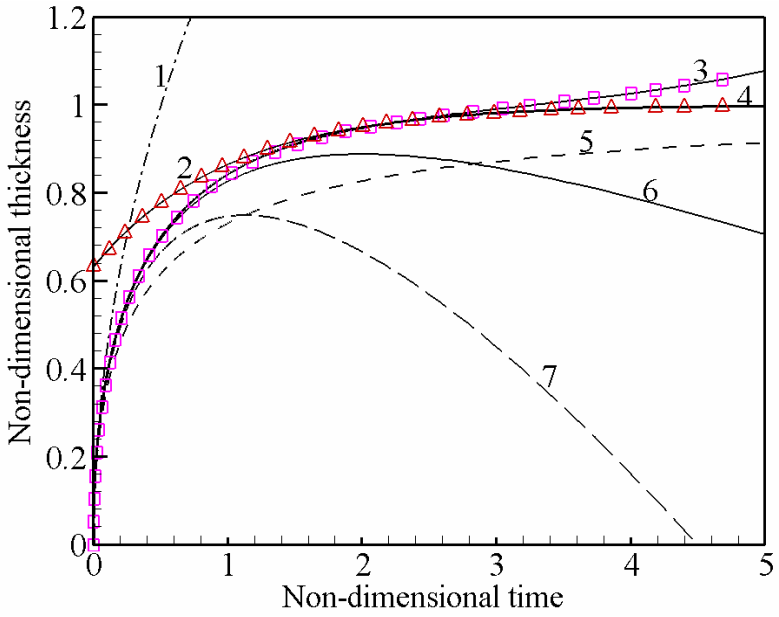

Figure 60. Variation of the non-dimensional thickness. (1) Pure parabolic oxide growth. (2) Asymptotic solution. (3) Perturbation solution up to the forth order. (4) Exact solution. (5) Haanappel et al. solution. (6) Perturbation solution up to the third order. (7) Perturbation solution up to the second order.

Corrosion Barrier Development for LBE Corrosion Resistance (Task 23).

Identification of alternate metal nanowires inside alumina template pores

As reported earlier, a significant problem was encountered with uniformity of Cr nanowires synthesized inside the alumina pores. A systematic study was carried out to improve the deposition uniformity, however no significant improvement could be achieved. This was a puzzling situation since a well established recipe was used for the deposition of Cr. The only explanation for the observed non-uniformity is the restricted space inside the nanopores that may not be amenable to the Cr synthesis chemistry. An FESEM image of a typical Cr nanowire inside the alumina template is shown in Figure 61, showing the non-uniformity of nanowire deposition.

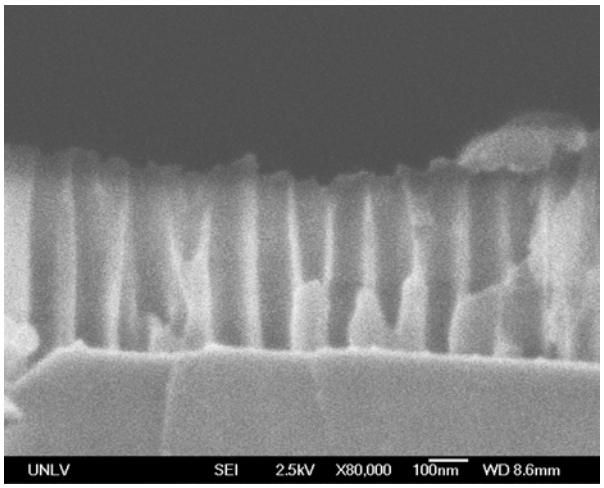

Figure 61. Cross-sectional FESEM image of Cr nanowires inside a porous alumina template showing nonuniform distrinution of nanowires.

As a solution to the above problem, alternative metals were investigated to form the nanowires. The purpose of the metal is to provide structural integrity to the nanoporous alumina, as well as a second defense mechanism against corrosion by oxidizing in case the top alumina layer is compromised. After a detailed search, Ni was selected as the metal to form the nanowires since (1) Ni nanowires have been demonstrated inside bulk alumina pores, and (2) Ni readily oxidizes to form a protective layer. For the deposition of Ni nanowires, the following reagent was purchased : Watts Ni Pure #130859 from Technic Inc. (Rhode Island). The reagent was used for the deposition of Ni inside the nanopores of the porous alumina template. The research group is currently waiting for SEM characterization of the samples.

Deposition of Ni nanoparticles inside alumina tremplate pores

In addition to the direct electrochemical deposition technique as described above, another approach to deposit Ni inside the nanopores was initiated. This technique involves the electrophoretic deposition of Ni nanoparticles inside the pores. Such Ni nanoparticles can be synthesized using established sol-gel techniques. A primary advantage of this technique is the improved flexibility of the Ni nanowires (consisting of nanoparticles) with thermal cycling. The design of a specialized sample holder shown in Figure 62 was completed to achieve this that is currently being fabricated. Once the apparatus is fabricated, the synthesis of the nanowires using the Ni nanoparticles will begin.

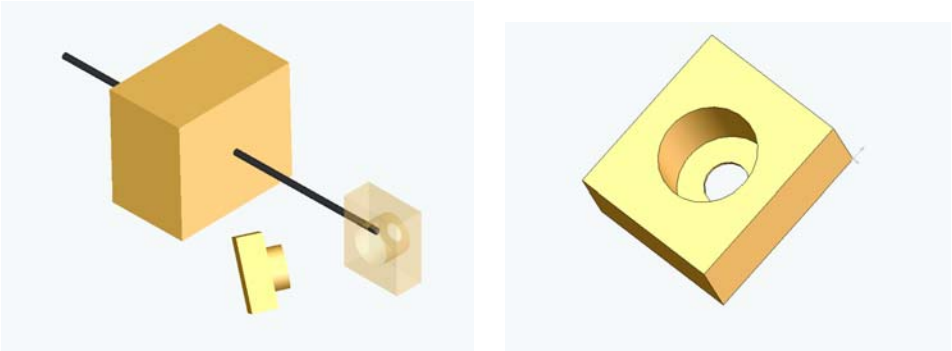

Figure 62. Specialized sample holder for the synthesis of nanowires using Ni nanoparticles.

Reactor Physics Studies for the AFCI RACE Project (Reactor-Accelerator Coupling Experiments Project (Task 27).

Undergraduate students completed a two-semester senior design project to design, construct, and test a new high-power, uranium-containing water-cooled target for Texas RACE. The design includes a tungsten electron-photon converter, an aluminum cooling shroud, and aluminum-clad natural uranium photon-neutron converter (Figure 63). Students gave their final design report for their senior design project for a water-cooled high power target for High-Power RACE. During their presentation they displayed rapid-prototype models of the target that they had fabricated in the UNLV machine shop (Figure 64). The models included mockups of separate tungsten, aluminum, and uranium components and a cut-away to demonstrate the machining and sealing of cooling channels.

A variety of code systems are being evaluated for modeling thermal feedback in accelerator-driven TRIGA reactors. ERANOS, RELAP, PARCS, and APOLLO were considered. The RELAP5 code system for thermal-hydraulic reactor analysis was received from INL and a license for the ERANOS/APOLLO code system for thermal-hydraulic reactor analysis from CEA (France).

Because of delays in the RACE Project at UT-Austin and ISU, the UNLV group is considering re-focusing UNLV RACE research to concentrate on a high-power target.

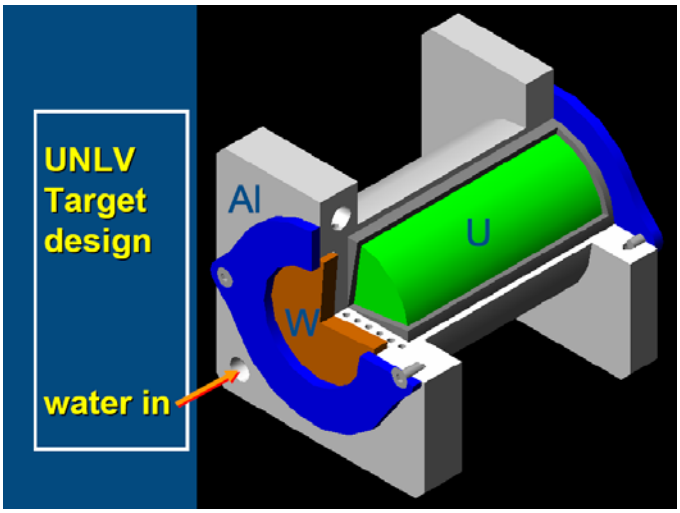

Figure 63. Conceptual design of a uranium-containing high-power target for Texas RACE.

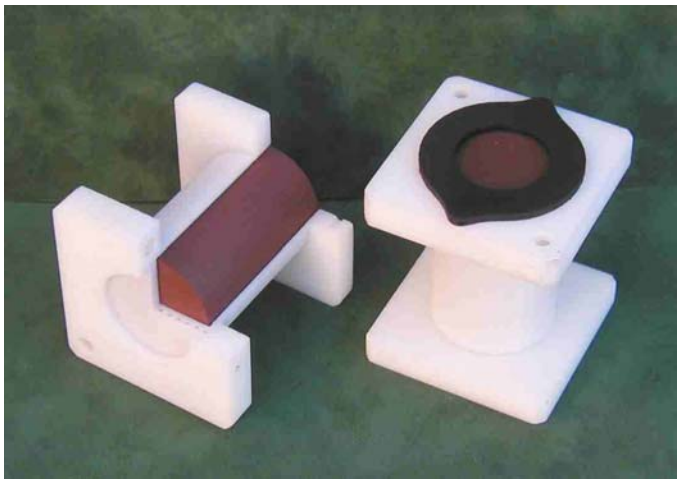

Figure 64. Rapid prototype models of the UNLV uranium-containing high-power target for Texas RACE.